ACADEMIC PRESS

Available online at www.sciencedirect.com

SCIENCE DIRECT®

Journal of Computational Physics 184 (2003) 498–525

JOURNAL OF COMPUTATIONAL PHYSICS

www.elsevier.com/locate/jcp

A WENO-solver for the transients of Boltzmann–Poisson system for semiconductor devices: performance and comparisons with Monte Carlo methods

José A. Carrillo [a], Irene M. Gamba [b], Armando Majorana [c], Chi-Wang Shu [d,*]

[a] *Departamento de Matemática Aplicada, Universidad de Granada, 18071 Granada, Spain*
[b] *Department of Mathematics, University of Texas at Austin, Austin, TX 78712, USA*
[c] *Dipartimento di Matematica e Informatica, Università di Catania, Catania, Italy*
[d] *Division of Applied Mathematics, Brown University, Providence, RI 02912, USA*

Received 20 February 2002; accepted 10 October 2002

Abstract

In this paper we develop a deterministic high order accurate finite-difference WENO solver to the solution of the 1-D Boltzmann–Poisson system for semiconductor devices. We follow the work in Fatemi and Odeh [9] and in Majorana and Pidatella [16] to formulate the Boltzmann–Poisson system in a spherical coordinate system using the energy as one of the coordinate variables, thus reducing the computational complexity to two dimensions in phase space and dramatically simplifying the evaluations of the collision terms. The solver is accurate in time hence potentially useful for time-dependent simulations, although in this paper we only test it for steady-state devices. The high order accuracy and nonoscillatory properties of the solver allow us to use very coarse meshes to get a satisfactory resolution, thus making it feasible to develop a 2-D solver (which will be five dimensional plus time when the phase space is discretized) on today's computers. The computational results have been compared with those by a Monte Carlo simulation and excellent agreements have been found. The advantage of the current solver over a Monte Carlo solver includes its faster speed, noise-free resolution, and easiness for arbitrary moment evaluations. This solver is thus a useful benchmark to check on the physical validity of various hydrodynamic and energy transport models. Some comparisons have been included in this paper.

Keywords: Boltzmann–Poisson system; WENO scheme; High order accuracy; Semiconductor devices

* Corresponding author. Tel.: 1-401-863-2549; fax: 1-401-863-1355.
E-mail addresses: carrillo@ugr.es (J.A. Carrillo), gamba@math.utexas.edu (I.M. Gamba), majorana@dmi.unict.it (A. Majorana), shu@dam.brown.edu (C.-W. Shu).

0021-9991/02/$ - see front matter
PII: S0021-9991(02)00032-3

1. Introduction

The Boltzmann transport equation (BTE) is the basis of the semiclassical description of charged particles flow in electronic devices. Based on statistical mechanics we study probabilities of charged particles in the phase space. The BTE for the evolution of a single carrier (electrons) in a semiconductor crystal [11,17] reads

$$\frac{\partial f}{\partial t} + \frac{1}{\hbar}\nabla_{\mathsf{k}}\varepsilon \cdot \nabla_{\mathsf{x}} f - \frac{\mathsf{e}}{\hbar}\mathsf{E} \cdot \nabla_{\mathsf{k}} f = Q(f), \tag{1}$$

where f is the electron probability density function, which depends on time t, space coordinates x and wavevector k. The parameters $\hbar$ and e are the Planck constant divided by 2π and the positive electric charge, respectively. We focus on a band structure with a single valley, if more valleys should be taken into account one ought to add additional equations of the type in Eq. (1) for the distribution of electrons in each valley.

The band structure of the semiconductor crystal is introduced by the energy-band function $\varepsilon(\mathsf{k})$. This function is taken usually as a correction of the parabolic-band approximation using the Kane dispersion relation and is given by

$$\varepsilon(\mathsf{k}) = \frac{1}{1 + \sqrt{1 + 2\frac{\tilde{\alpha}}{m^*}\hbar^2|\mathsf{k}|^2}} \frac{\hbar^2}{m^*}|\mathsf{k}|^2, \tag{2}$$

where m^* is the effective mass and $\tilde{\alpha}$ is the nonparabolicity factor. The parabolic-band approximation is obtained from Eq. (2) by setting $\tilde{\alpha}$ to 0.

We are modeling electrons moving in the same symmetry-type of valleys and then f represents an average probability density function (pdf) among these analogous valleys. Therefore, we neglect intervalley scatterings and we consider only intravalley scattering mechanisms.

These collisions are due to the thermal bath of phonons produced by the semiconductor crystal. We will consider two types of scattering mechanisms: acoustic phonon scattering in the elastic approximation and optical nonpolar phonon scattering with a single frequency ω. Therefore, the specific structure of the collision operator (see [19,27]) based on the semiclassical approach to scattering mechanisms is given by

$$Q(f)(t,\mathsf{x},\mathsf{k}) = \int_{\mathbb{R}^3} \Big[S(\mathsf{k}',\mathsf{k})f(t,\mathsf{x},\mathsf{k}') - S(\mathsf{k},\mathsf{k}')f(t,\mathsf{x},\mathsf{k})\Big]\,\mathrm{d}\mathsf{k}' \tag{3}$$

with

$$S(\mathsf{k},\mathsf{k}') = K_0(\mathsf{k},\mathsf{k}')\delta(\varepsilon(\mathsf{k}') - \varepsilon(\mathsf{k})) + K(\mathsf{k},\mathsf{k}')\Big[(\mathsf{n}_q + 1)\delta(\varepsilon(\mathsf{k}') - \varepsilon(\mathsf{k}) + \hbar\omega) + \mathsf{n}_q\delta(\varepsilon(\mathsf{k}') - \varepsilon(\mathsf{k}) - \hbar\omega)\Big], \tag{4}$$

where the constant n_q is the occupation number of phonons given by

$$\mathsf{n}_q = \left[\exp\left(\frac{\hbar\omega}{k_{\mathrm{B}}T_{\mathrm{L}}}\right) - 1\right]^{-1},$$

where k_{B} is the Boltzmann constant and T_{L} is the lattice temperature. The symbol δ indicates the usual Dirac distribution. The exact meaning of $Q(f)$ will be clarified below. Let us finally point out that this choice of scattering mechanisms and band structure is not arbitrary since they are the right choice for the Si devices.

Eq. (1) is obtained through a mean-field type approximation and thus, the electric field is computed self-consistently from the density of electrons

$$\rho(t,\mathsf{x}) = \int_{\Re^3} f(t,\mathsf{x},\mathsf{k})\,\mathrm{d}\mathsf{k}$$

through the Poisson equation

$$\Delta V = \frac{\mathfrak{e}}{\epsilon}[\rho(t,\mathsf{x}) - N_{\mathrm{D}}(\mathsf{x})], \tag{5}$$

$$\mathsf{E} = -\nabla_{\mathsf{x}} V, \tag{6}$$

where ϵ is the permittivity, $N_{\mathrm{D}}(\mathsf{x})$ is the doping profile and V is the electric potential. The doping profile takes into account the impurities due to acceptor and donor ions in the semiconductor device. Eqs. (1), (5) and (6) are the Boltzmann–Poisson (BP) system for semiconductors.

Semiclassical description of electron flow in semiconductors needs therefore an evolution solver in six dimensions (plus time if the device is not in steady state) for a truly 3-D device, five dimensions for a 2-D device and in principle four dimensions for a 1-D device. This heavy computational cost is one of the reasons why the BP system is usually simulated using Direct Simulation Monte Carlo (DSMC) methods.

The main advantage of DSMC is the simplicity to introduce the various scattering mechanisms and the electron energy band structure. In principle, the description of the electron dynamics is very simple. An electron moves inside the device subject only to the mean electric field (drift process). After a small time step (mean free time) a random number is drawn and a scattering effect between electron and phonons is modeled depending on the random value. The two procedures are called until a given predetermined fixed time t_1. Unfortunately, the reconstruction of the distribution function, at a fixed time t_1 from the knowledge of position and velocity of the particles used in the simulation, requires the use of an average. In fact, the only way to obtain a reasonable distribution function with reduced noise is to have a large number of particles in the interval $(t_1 - n \times \Delta t, t_1 + n \times \Delta t)$ and to choose the number n large enough for the averaging. Of course, the choice of n depends on the number of particles and also on the proximity to an equilibrium state. One consequence of this is that transient processes are described poorly.

Therefore, a deterministic computation of transients and steady states for the BP system, if possible, is more reliable than DSMC methods due to the stochastic nature of the latter.

The numerical scheme proposed here for the full Boltzmann–Poisson system yields deterministic numerical results for each time step. It is useful to compare with, not only in the stationary case but also in time transient, results obtained using different kinetic or hydrodynamic models. For example, in [15] space homogeneous solutions of the BP system are compared with results obtained using the kinetic equations (SHE), which are derived from the Boltzmann equation using the spherical harmonic expansion [18]. There is a good agreement in the stationary case. However when strong time gradients occur, the SHE gives unsatisfactory and in some cases nonphysical results. Hence, BP simulations can better test and validate new kinetic or hydrodynamic models.

It is important to notice that today's realistic simulations of three dimensional devices can be obtained only using simple models, however the simplest, widely used Drift-Diffusion-Poisson (DDP) model gives wrong results in the presence of high electric fields.

In this paper we follow the trend towards deterministic reliable solvers for the BP system focusing on the 1-D case. This case due to its cylindrical symmetry can be reduced to an evolution in three dimensions (position, energy, angle with respect to the force field direction axis). This was first attempted by Fatemi and Odeh [9]. They wrote the BP system in the parabolic-band approximation in spherical coordinates and solved the resulting hyperbolic equation using simple first order upwinding methods for the space–momentum variables with predictor-corrector type methods for the time evolution. Moreover, due to the singularity of the change of variables they had to take out a small neighborhood of the origin in the

momentum space with heuristic boundary conditions. Recently, Majorana and Pidatella [16] introduced a new change of variables valid also for the nonparabolic band case in which the BP system becomes a conservation law and thus, simpler than that in [9]. Based on this change of variables, Majorana and Pidatella solved the BP system by a combination of a box method in energy and angle variables and classical discretization methods for advection equations based on upwinding in the spatial variable. Time evolution was done by means of implicit predictor-corrector methods. A main advantage of the approach in [16] is that it has dramatically simplified the evaluations of the collision terms.

In the present paper, we improve the numerical discretization in [16]. The key point is that the change of variables in [16] translates the BP system into a conservation law in conservative form with a right-hand side collision term that can be easily evaluated. This conservation law is linear if we disregard the coupling with Poisson equation. Furthermore, we know that typically in these devices we have regions of very strong steep spatial gradients due to the existence of sharp discontinuous doping profiles. Linear high order upwind methods are known to produce very oscillatory approximations in the vicinity of these regions. On top of this we would like to have a fast solver in time, purely explicit if possible. This would save the storage space for the solver and would be a key ingredient if one wants to generalize the solver to 2-D (five dimensions plus time when the phase space is discretized). Based on all the above considerations, we have decided to use a very robust solver for nonlinear conservation laws that is very accurate for smooth solutions but at the same time keeps the nonoscillatory character near shocks or steep gradients regions. The high order method we use is the fifth order WENO (weighted essentially nonoscillatory) scheme that has been used extensively in different applications [13,25]. Due to its nonoscillatory character we are able to use a third order TVD Runge–Kutta explicit method [26] for the time marching algorithm. Therefore, we present here a space–time accurate fully finite-difference method for the BP system in 1-D. Advantages over DSMC methods for 1-D are: lower computational cost, noise-free resolution, capability of capturing transients and studying relaxation to steady states, and explicit computation of the pdf f in the devices and hence all the moments.

Let us mention that another deterministic approach has been derived very recently for the BP system in 1-D. This approach is based on series expansion methods for the Boltzmann equation introduced in [20] and references therein. This Galerkin type method is used in the momentum variable and leads to a hyperbolic system solved by suitable finite-differences methods in space–time variables [21,22]. Moreover, a direct solver for the steady-state case has been developed by C. Ringhofer in [23]. Our present solver can be used for studying steady states by marching in time until stabilization (see Section 3) but may be slower than a direct steady-state solver like the one in [23]. Nevertheless, an explicit time-dependent solver is important to analyze transients and has less complexity and a smaller storage requirement, hence it might have its advantage over direct steady-state solvers in more than one dimension. Finally, we want to mention another deterministic approach: particle methods which in some sense can be considered as a middle ground between DSMC methods and finite-difference methods. They were used for the BP system for semiconductors in [7,8] with the cylindrical symmetry assumption in 1-D but working with parallel and orthogonal velocities to the electron flow axis rather than changing to the spherical coordinate system. Although this approach makes it plausible to obtain pdf plots of the distribution functions for homogeneous regimes, it encounters difficulties in doing so in inhomogeneous situations in which only angle-averaged pdf's are well resolved. Also, the results obtained are noisy in nature (although less noisy than the DSMC results) due to the approximation of the pdf by a combination of Dirac δ distributions which is the basis of the method.

The plan of this paper is the following: in Section 2 we review the change of variables in [16] and we explain the numerical discretization of the resulting system. The rest of the paper is devoted to simulation and comparison results with other simplified models introduced in the literature. Section 3 focuses on steady-state results for different diodes: pdf and IV-curves are obtained. The time evolution and relaxation towards steady state in these diodes are the objectives of Section 4. Section 5 is devoted to comparisons between the results given by the BP system using our deterministic solver for steady state in

diodes and the results given by other classical approximations such as: drift-diffusion, hydrodynamic models, kinetic relaxation models, and DSMC results.

2. WENO finite-difference method for the BP system

First we obtain a suitable dimensionless formulation in spherical coordinates of the BP system, following [16]. We then explain our numerical discretization of the BP system based on WENO methods for conservation laws.

2.1. The BP system in energy-band-adapted coordinates

Let us consider the coordinate transformation

$$\mathsf{k} = \sqrt{2}\frac{\sqrt{m^* k_B T_L}}{\hbar}\sqrt{w}\sqrt{1+\alpha_K w}\left(\sqrt{1-\mu^2}\cos\phi, \sqrt{1-\mu^2}\sin\phi, \mu\right), \tag{7}$$

where $\alpha_K = k_B T_L \tilde{\alpha}$, w is a dimensionless energy, μ is the cosine of the angle between the wavevector k and the z-axis and ϕ is the polar angle. We will consider our device in the z-direction with $\mathrm{x} = (x, y, z)$ by assuming that the doping profile and the potential and thus, the force field are only z-dependent.

The advantages of the change of variables are that due to the cylindrical symmetry the resulting distribution function does not depend on ϕ and the collision operator $Q(f)$ is easily evaluated since all the integrals involving δ functions are explicitly computed due to the fact that energy $\varepsilon = k_B T_L w$ has become a variable in the new coordinate system.

Let K_* be a dimensional constant parameter of the *same order* as the kernel K. Here we put a tilde over the dimensional variables. Let us consider the following set of dimensionless variables:

$$\alpha = \frac{\hbar\omega}{k_B T_L}, \quad a = \frac{n_q + 1}{n_q} = e^{\alpha},$$

$$\tilde{K}(\mathsf{k}, \mathsf{k}') = K_* K(\xi, \xi'), \quad \tilde{K}_0(\mathsf{k}, \mathsf{k}') = K_* n_q K_0(\xi, \xi'),$$

$$t_* = \left[4\sqrt{2}\pi\frac{m^*\sqrt{m_*}}{\hbar^3}\sqrt{k_B T_L}\, n_q K_*\right]^{-1}, \quad l_* = \sqrt{\frac{k_B T_L}{m^*}}\, t_*,$$

$$\tilde{t} = t_* t, \quad \tilde{\mathbf{x}} = \sqrt{2} l_* \mathbf{x},$$

$$\tilde{N}_D(\tilde{\mathbf{x}}) = \left(\frac{\sqrt{2m^* k_B T_L}}{\hbar}\right)^3 N_D(\mathbf{x}), \quad c_p = \frac{2\sqrt{2}}{\epsilon}\mathfrak{e}^2 l_*^2 \frac{m^*\sqrt{m^*}}{\hbar^3}\sqrt{k_B T_L},$$

$$\tilde{\mathbf{E}}(\tilde{t}, \tilde{\mathbf{x}}) = \sqrt{2}\frac{k_B T_L}{\mathfrak{e} l_*}\mathbf{E}(t, \mathbf{x}), \quad V(\tilde{t}, \tilde{\mathbf{x}}) = 2\frac{k_B T_L}{\mathfrak{e}}\Psi(t, \mathbf{x}),$$

where $\xi = (w, \phi, \mu)$. Here z is the spatial coordinate and t is the dimensionless time.

Following [16] we choose for Si devices the value of K_* in order to have

$$K = 1 \quad \text{and} \quad K_0 = \beta \simeq 5.986,$$

and then, $t_* \simeq 3.6\,\text{ps}$ and $l_* \simeq 0.43\,\mu\text{m}$.

Specifically, given m_0 the electron mass, ρ_0 the crystal density, $D_t k$ the optical coupling constant, u_l the sound velocity and E_{ac} the deformation potential, we consider the following table for the numerical values involved:

$\hbar\omega = 0.063\,\mathrm{eV}$	$T_\mathrm{L} = 300\,\mathrm{K}$
$\tilde{\alpha} = 0.5\,(\mathrm{eV})^{-1}$	$\rho_0 = 2330\,\mathrm{K\,g\,m^{-3}}$
$\epsilon_0 = 8.85419 \times 10^{-12}\,\mathrm{F\,m^{-1}}$	$\epsilon = 11.7 \cdot \epsilon_0$
$m_* = 0.32 \cdot m_0$	$u_l = 9040\,\mathrm{ms^{-1}}$
$D_t k = 11.4 \times 10^{10}\,\mathrm{eV\,m^{-1}}$	$E_{ac} = 9\,\mathrm{eV}$
$\tilde{K} = D_t k^2/(8\pi^2\rho_0\omega)$	$\tilde{K}_0 = k_\mathrm{B} T_\mathrm{L} E_{ac}^2/(4\pi^2\hbar u_l^2\rho_0)$
$\alpha = 2.43694,$	$a = 11.438$
$\beta = 5.986$	$K_* = 1.89405 \times 10^{-35}$
$n_q = 0.0958036$	

In terms of the new variables the unknown f is denoted by F. Let

$$s(w) = \sqrt{w(1+\alpha_K w)}(1+2\alpha_K w),$$

$$\Phi(t,z,w,\mu) = s(w)F(t,z,w,\mu). \tag{8}$$

The function Φ will be the new unknown. The function $s(w)$ is proportional to the Jacobian of the coordinate transformation and thus, we can evaluate moments of the distribution function directly from Φ. The collision operator in terms of Φ becomes

$$C(\Phi) = \frac{1}{2}\int_{-1}^{1}[\beta\Phi(t,z,w,\mu') + a\Phi(t,z,w+\alpha,\mu') + \Phi(t,z,w-\alpha,\mu')]\,\mathrm{d}\mu' - \frac{1}{s(w)}[\beta s(w) + as(w-\alpha) + s(w+\alpha)]\Phi(t,z,w,\mu). \tag{9}$$

The variables are

$$z \in [0,L], \quad w \in [0,w_{\max}], \quad \mu \in [-1,1],$$

where L is the dimensionless length of the device and $w_{\max} = \bar{N}\alpha$ is the maximum value of the energy, which is adjusted in the numerical experiments such that

$$F(t,z,w,\mu) \simeq 0 \quad \text{for } w \geqslant w_{\max} \quad \text{for every } t,z,\mu.$$

As in [16] a cut was introduced in the collision operator in order to guarantee the mass conservation also in the numerical approximation. Poisson equation translates into

$$\frac{\partial^2\Psi}{\partial z^2} = -c_p\left[N_\mathrm{D}(z) - \pi\int_0^{+\infty}\mathrm{d}w\int_{-1}^{1}\mathrm{d}\mu\,\Phi(t,z,w,\mu)\right]. \tag{10}$$

Finally, the BTE equation (1) in conservation form translates into

$$\frac{\partial\Phi}{\partial t} + \frac{\partial}{\partial z}(a_1\Phi) + \frac{\partial}{\partial w}(a_2\Phi) + \frac{\partial}{\partial\mu}(a_3\Phi) = s(w)C(\Phi), \tag{11}$$

where the fluxes are linear in the f variable but variable dependent and given by

$$a_1 = a_1(w,\mu) = \frac{\mu s(w)}{(1+2\alpha_K w)^2}, \tag{12}$$

$$a_2 = a_2(t,z,w,\mu) = -E(t,z)\frac{2\mu s(w)}{(1+2\alpha_K w)^2}, \tag{13}$$

and

$$a_3 = a_3(t,z,w,\mu) = -E(t,z)\,\frac{(1-\mu^2)(1+2\alpha_K w)}{s(w)} \tag{14}$$

with $E(t,z) = -\partial_z \Psi$.

Let us remark that the coefficients in the fluxes, a_1 and a_2 are completely smooth assuming E is given and smooth, in the variables w and μ. However, a_3 is singular for the zero energy $w = 0$, although the $s(w)$ factor in the definition of Φ should compensate this singularity.

The initial value of Φ is a locally Maxwellian distribution at the temperature T_{L}

$$\Phi(0,z,w,\mu) = \mathscr{M} s(w) N_{\mathrm{D}}(z)\,\mathrm{e}^{-w}$$

with $\mathscr{M}$ chosen so that the initial value for the density is equal to the doping $N_{\mathrm{D}}(z)$.

2.2. Numerical scheme

Equation (11) is solved by the fifth order conservative finite difference WENO scheme [13] coupled with a third order TVD Runge–Kutta time discretization [26]. The computational domain is discretized into a tensor product mesh, and a uniform mesh is taken in each direction:

$$\begin{aligned} &z_i = (i-1/2)\Delta z; \quad i = 1,2,\ldots,N_z,\\ &w_j = (j-1/2)\Delta w; \quad j = 1,2,\ldots,N_w,\\ &\mu_k = -1+(k-1/2)\Delta\mu; \quad k = 1,2,\ldots,N_\mu, \end{aligned} \tag{15}$$

where $\Delta z = L/N_z$, $\Delta w = w_{\max}/N_w$, and $\Delta\mu = 2/N_\mu$ are the mesh sizes in each direction. Notice that $w_{\max}$ is chosen as an integer multiple of α in (9), and Δw is chosen as $\alpha/n_{\mathrm{multiple}}$ where n_{multiple} is an integer related to the resolution in the w direction for the collision term. These choices are taken in order to make the evaluations of the collision operator in (9) easy without any smearing to the δ function. All the values in the calculation of the collision terms in (9) are located at grid points and thus will not involve any interpolations. The WENO solver also allows a smooth nonuniform mesh which could concentrate points in specified locations. Notice that the boundaries $w = 0$ and $\mu = \pm 1$ are not grid points, rather they are half a mesh size away from the first computational grid point. This setup is important for the implementation of symmetry type boundary conditions.

The approximations to the point values of the solution $\Phi(t^n, z_i, w_j, \mu_k)$, denoted by $\Phi^n_{i,j,k}$, are obtained with a dimension by dimension (not dimension splitting) approximation to the spatial derivatives using fifth order WENO method in [13]. When approximating $\frac{\partial}{\partial z}(a_1\Phi)$, for example, the other two variables w and μ are fixed and the approximation is performed along the z-line:

$$\frac{\partial}{\partial z}\left(a_1(w_j,\mu_k)\Phi(t^n,z_i,w_j,\mu_k)\right) \approx \frac{1}{\Delta z}\left(\hat{h}_{i+1/2} - \hat{h}_{i-1/2}\right),$$

where the numerical flux $\hat{h}_{i+1/2}$ is obtained with the following procedure. Notice that the "wind direction," namely the sign of the coefficient $a_1(w_j,\mu_k)$, is independent of i. Thus when j and k are fixed, the wind direction is fixed for all i. Let us assume, without loss of generality, that $a_1(w_j,\mu_k) > 0$, for otherwise the procedure would just be a mirror symmetry with respect to $i+1/2$ when computing $\hat{h}_{i+1/2}$. We denote by

$$h_i = a_1(w_j,\mu_k)\Phi(t^n,z_i,w_j,\mu_k), \quad i = -2,-1,\ldots,N_z+2,$$

where j, k, and n are all fixed. We obtain the numerical flux by

$$\hat{h}_{i+1/2} = \omega_1 \hat{h}^{(1)}_{i+1/2} + \omega_2 \hat{h}^{(2)}_{i+1/2} + \omega_3 \hat{h}^{(3)}_{i+1/2},$$

where $\hat{h}^{(m)}_{i+1/2}$ are the three third order fluxes on three different stencils given by

$$\hat{h}^{(1)}_{i+1/2} = \frac{1}{3}h_{i-2} - \frac{7}{6}h_{i-1} + \frac{11}{6}h_i,$$

$$\hat{h}^{(2)}_{i+1/2} = -\frac{1}{6}h_{i-1} + \frac{5}{6}h_i + \frac{1}{3}h_{i+1},$$

$$\hat{h}^{(3)}_{i+1/2} = \frac{1}{3}h_i + \frac{5}{6}h_{i+1} - \frac{1}{6}h_{i+2},$$

and the nonlinear weights ω_m are given by

$$\omega_m = \frac{\tilde{\omega}_m}{\sum_{l=1}^{3}\tilde{\omega}_l}, \quad \tilde{\omega}_l = \frac{\gamma_l}{(\varepsilon + \beta_l)^2},$$

with the linear weights γ_l given by

$$\gamma_1 = \frac{1}{10}, \quad \gamma_2 = \frac{3}{5}, \quad \gamma_3 = \frac{3}{10},$$

and the smoothness indicators β_l given by

$$\beta_1 = \frac{13}{12}(h_{i-2} - 2h_{i-1} + h_i)^2 + \frac{1}{4}(h_{i-2} - 4h_{i-1} + 3h_i)^2,$$

$$\beta_2 = \frac{13}{12}(h_{i-1} - 2h_i + h_{i+1})^2 + \frac{1}{4}(h_{i-1} - h_{i+1})^2,$$

$$\beta_3 = \frac{13}{12}(h_i - 2h_{i+1} + h_{i+2})^2 + \frac{1}{4}(3h_i - 4h_{i+1} + h_{i+2})^2.$$

Finally, ε is a parameter to avoid the denominator to become 0 and is taken as $\varepsilon = 10^{-6}$ in the computation of this paper.

Approximations to $\frac{\partial}{\partial w}(a_2\Phi)$ and $\frac{\partial}{\partial \mu}(a_3\Phi)$ are performed in the same fashion. Notice that again the "wind direction" is fixed (i.e. the sign of a_2 is fixed when z_i and μ_k are fixed, and the sign of a_3 is fixed when z_i and w_j are fixed), which allows us to use the same simple procedure outlined above.

This finishes the description of the fifth order finite-difference WENO scheme [13] in the current simple case. As we can see, the algorithm is actually quite simple and there are no parameters to be tuned in the scheme.

Next we describe the boundary conditions:

- At $z = 0$ and $z = L$, we use the standard inflow/outflow boundary conditions. For the 1-D diodes tested in this paper, the result is not sensitive to the boundary conditions at $z = 0$ and $z = L$. Thus, we choose to implement a reflective boundary condition at $z = 0$ and $z = L$. If $a_1 \geqslant 0$, then

  $$\Phi_{1-i,j,k} = \Phi_{i,j,k}, \quad \Phi_{N_x+i,j,k} = \Phi_{N_x,j,k}, \quad i = 1, \ldots, 3,$$

  otherwise if $a_1 < 0$, then

  $$\Phi_{1-i,j,k} = \Phi_{1,j,k}, \quad \Phi_{N_x+i,j,k} = \Phi_{N_x-i+1,j,k}, \quad i = 1, \ldots, 3,$$

  namely reflection is enforced for inflows and Neumann type boundary condition is implemented for outflows.

- At $w = 0$, the boundary condition is given to take into consideration that this is not really a physical boundary, a "ghost point" at (w, μ) for negative w actually is a physical point at $(-w, -\mu)$. We thus take the boundary condition as

$$\Phi_{i,1-j,k} = \Phi_{i,j,N_\mu+1-k}, \quad j = 1, \ldots, 3.$$

  Since μ appears linearly in a_2, the numerical flux $\hat{h}_{1/2}$ in the j direction at $w = 0$ for a given μ should be exactly of the same value and opposite sign as the numerical flux $\hat{h}_{1/2}$ in the j direction at $w = 0$ for $-\mu$, if a central, linear numerical flux formula is taken. Since we use upwind biased WENO, this exact equality does not hold anymore. To enforce conservation of mass, we average these two fluxes at $w = 0$ and use the averaged flux for both μ and $-\mu$ with opposite signs.
- $w = w_{\max}$ is taken as an outflow boundary, with a Neumann type boundary condition

$$\Phi_{i,N_w+j,k} = \Phi_{i,N_w,k}, \quad j = 1, \ldots, 3,$$

  and the explicit enforcement of $\hat{h}_{N_w+1/2} = 0$ for the last numerical flux in order to enforce conservation of mass.
- At $\mu = -1$ and $\mu = 1$, we take the boundary conditions as

$$\Phi_{i,j,1-k} = \Phi_{i,j,k}, \quad \Phi_{i,j,N_\mu+k} = \Phi_{i,j,N_\mu-k+1}, \quad k = 1, \ldots, 3,$$

  motivated by the physical meaning of μ as the cosine of the angle to the z-axis. We also explicitly impose $\hat{h}_0 = \hat{h}_{N_\mu+1/2} = 0$ for the first and last numerical fluxes in order to enforce conservation of mass.

An integration to compute the various moments using the pdf is approximated by the composite midpoint rule:

$$\int_0^{+\infty} \mathrm{d}w \int_{-1}^{1} \mathrm{d}\mu\, b(w,\mu)\Phi(t,z,w,\mu) \approx \sum_{k=1}^{N_\mu} \sum_{j=1}^{N_w} b(w_j,\mu_k)\Phi(t,z,w_j,\mu_k)\Delta w \Delta\mu,$$

which is at least second order accurate, and is more accurate when Φ is 0 at the boundaries together with more of its derivatives—in fact it is infinite order accurate, or spectrally accurate for C^∞ functions with compact support. Notice that a mass conservation is enforced with this integration formula and the boundary conditions taken before.

The Poisson equation (10) for the potential Ψ and the electric field $E = -\partial_z \Psi$ are solved by the standard central difference scheme, with the given V_{bias} boundary conditions.

The time discretization is by the following third order TVD Runge–Kutta method [26]:

$$\begin{aligned}
\Phi^{(1)} &= \Phi^n + \Delta t L(\Phi^n, t^n),\\
\Phi^{(2)} &= \frac{3}{4}\Phi^n + \frac{1}{4}\Phi^{(1)} + \frac{1}{4}\Delta t L(\Phi^{(1)}, t^n + \Delta t),\\
\Phi^{n+1} &= \frac{1}{3}\Phi^n + \frac{2}{3}\Phi^{(2)} + \frac{2}{3}\Delta t L\left(\Phi^{(2)}, t^n + \frac{1}{2}\Delta t\right),
\end{aligned}$$

where L is the approximation to the spatial derivatives and the collision terms:

$$L(\Phi, t) \approx -\left(\frac{\partial}{\partial z}(a_1\Phi) + \frac{\partial}{\partial w}(a_2\Phi) + \frac{\partial}{\partial \mu}(a_3\Phi)\right) + s(w)C(\Phi).$$

Again, notice that all the values in the calculation of the collision terms in (9) are located at grid points and thus will not involve any interpolations. We remark that this time discretization only needs three storage

units per grid point, two for Φ and one for L. For a 2-D solver (to be developed in the future), storage will be a paramount consideration, thus we will use the TVD low storage third order Runge–Kutta method in [10].

Finally, due to the explicit character of the time evolution solver we need to impose the standard CFL condition for these RK schemes (see [25] for a discussion), that is,

$$\Delta t \leqslant \mathrm{CFL}\left(\frac{\Delta z}{\max(|a_1|)} + \frac{\Delta w}{\max(|a_2|)} + \frac{\Delta \mu}{\max(|a_3|)}\right),$$

where the maximum is taken over the grid points. Note we are taking $\max(|a_3|)$ over a grid without $w = 0$. For the cases we have run, the source collision term is not stiff enough to change the CFL condition determined by the approximations to the spatial derivatives. This CFL condition at first glance may seem severe, however practical cases shown in next sections demonstrate this is not the case and in fact, CPU time is much lower than for DSMC simulations.

3. Steady-state results for the diodes

We consider two test examples: Si n^+–n–n^+ diodes of a total length of 1 and 0.25 μm, with 400 and 50 nm channels located in the middle of the device, respectively.

For the 400 nm channel device the dimensional doping is given by $N_D = 5 \times 10^{17}\,\mathrm{cm}^{-3}$ in the n^+ region and $N_D = 2 \times 10^{15}\,\mathrm{cm}^{-3}$ in the n region. The grid we use for all the results in this case is $150 \times 40 \times 16$. Also $n_{\mathrm{multiple}} = 4$.

For the 50 nm one, $N_D = 5 \times 10^{18}\mathrm{cm}^{-3}$ in the n^+ region and $N_D = 1 \times 10^{15}\mathrm{cm}^{-3}$ in the n region. The grid in this case is $150 \times 144 \times 16$, except for the parabolic band cases with V_{bias} larger than 1 V where we have used 200 points in the w direction to increase the numerical support in that direction. Also $n_{\mathrm{multiple}} = 8$.

The grids chosen give a converged resolution to a visual inspection for the quantities we are interested in, verified by grid refinements. We will comment later on the resolution of even coarser grids. We consider these two test cases with these values of the doping since they have served as references in many other works in this area during the last few years [5,9,16,23,24]. By conventional wisdom, the first case is expected to be close to a local equilibrium (shift Maxwellians and their expansions) due to the small jump in the doping and hence is expected to have small mean free path. However, the second case is considered to be an example which captures out-of-equilibrium distributions and should show purely kinetic effects which are not captured by expansions about local equilibria (drift-diffusion like models, classical hydrodynamic models, etc.) or by spherical harmonic expansion models (SHE models, etc.). All results plotted are at the $V_{\mathrm{bias}} = 1\,\mathrm{V}$, except for the IV-curves which show relationships between current and voltage bias.

Figs. 1 and 2 show a sequence of pdf's in the z-direction at locations specified on the captions. We can see how the pdf changes from being Maxwellian distributions at the contact to shifted distributions along the channel and finally, it recovers its original Maxwellian shape after the second junction. Also, we can verify numerically the fact that the distribution function is relatively not far from being an shifted Maxwellian (corresponding to a diffusion approximation) in the 400 nm case (see Fig. 1 at $z_0 = 0.5\,\mu\mathrm{m}$ and $z_0 = 0.6\,\mu\mathrm{m}$). However, we can realize that this is no longer the case in the 50 nm channel test, for higher potential bias. The pdf in Fig. 2 at $z_0 = 0.125\,\mu\mathrm{m}$ and $z_0 = 0.150\,\mu\mathrm{m}$ shows the formation of a very asymmetric distribution function with a moderately populated tail that demonstrates purely kinetic features, which is clearly far from shifted Maxwellians. In order to support this claim we show the pdf at the center of the channel in both cases in Cartesian coordinates in Figs. 3 and 4. Here we just obtained the Cartesian coordinate pdf function in terms of Φ by the change of variables (7). The coordinate variables in the plot are the

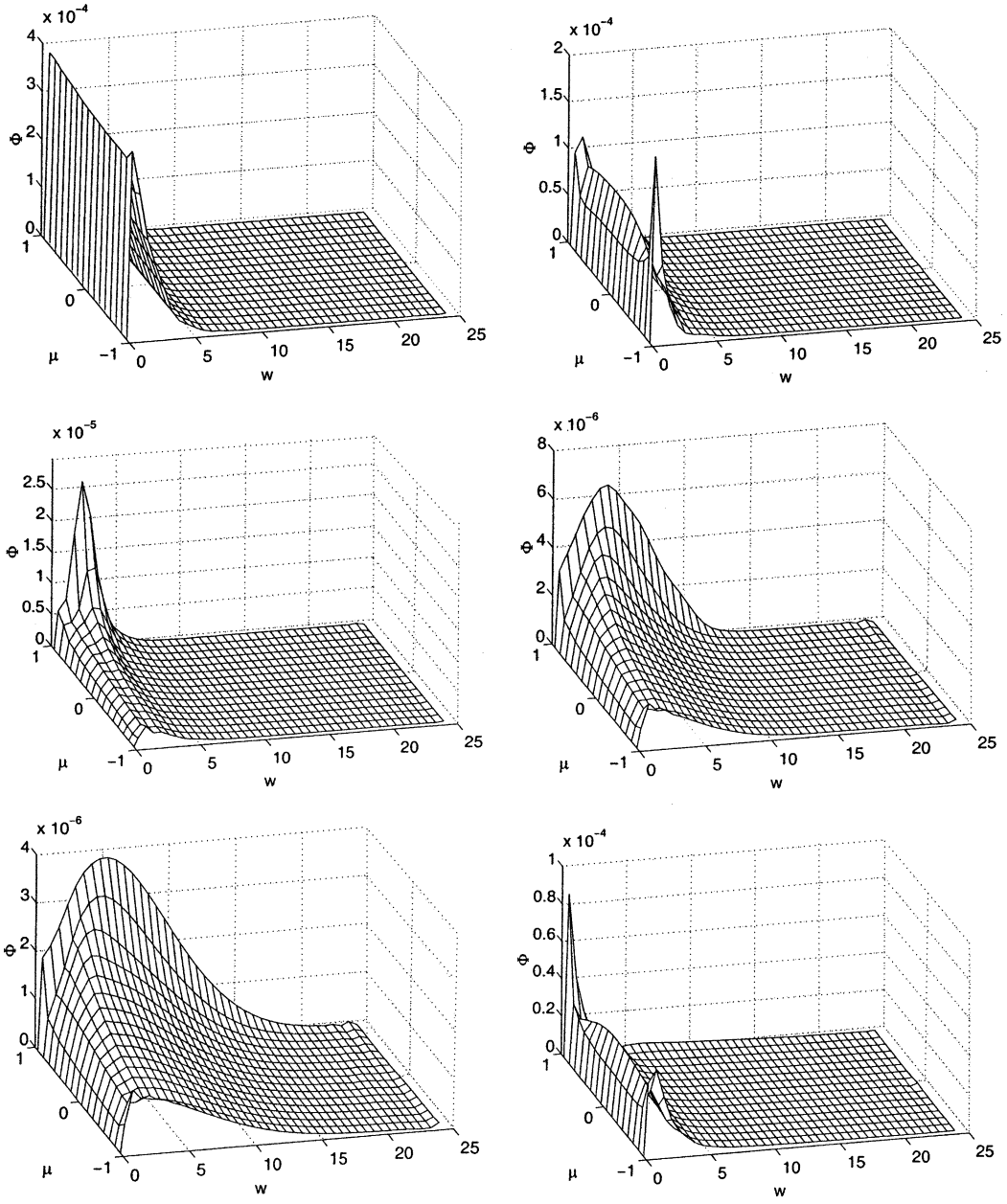

Fig. 1. Spatial snapshots of the steady-state pdf $\Phi_\infty(z_0, w, \mu)$ for the 400 nm channel with 1 V V_{bias}. From left to right and from top to bottom at $z_0 = 0.1$, 0.3, 0.4, 0.5, 0.6, and 0.7 μm.

component of the momentum parallel to the force field k_3 and the modulus of the orthogonal component. We point out that pdf's in terms of k_3 averaged over its orthogonal component are the best noise-free results one could obtain from particle method codes in [7,8]. Here we realize one of the advantages of this method to other approaches, namely we can obtain a reliable approximation of the pdf and then of all the moments at each location of the device. This is also the case with the direct steady-state solver in [23].

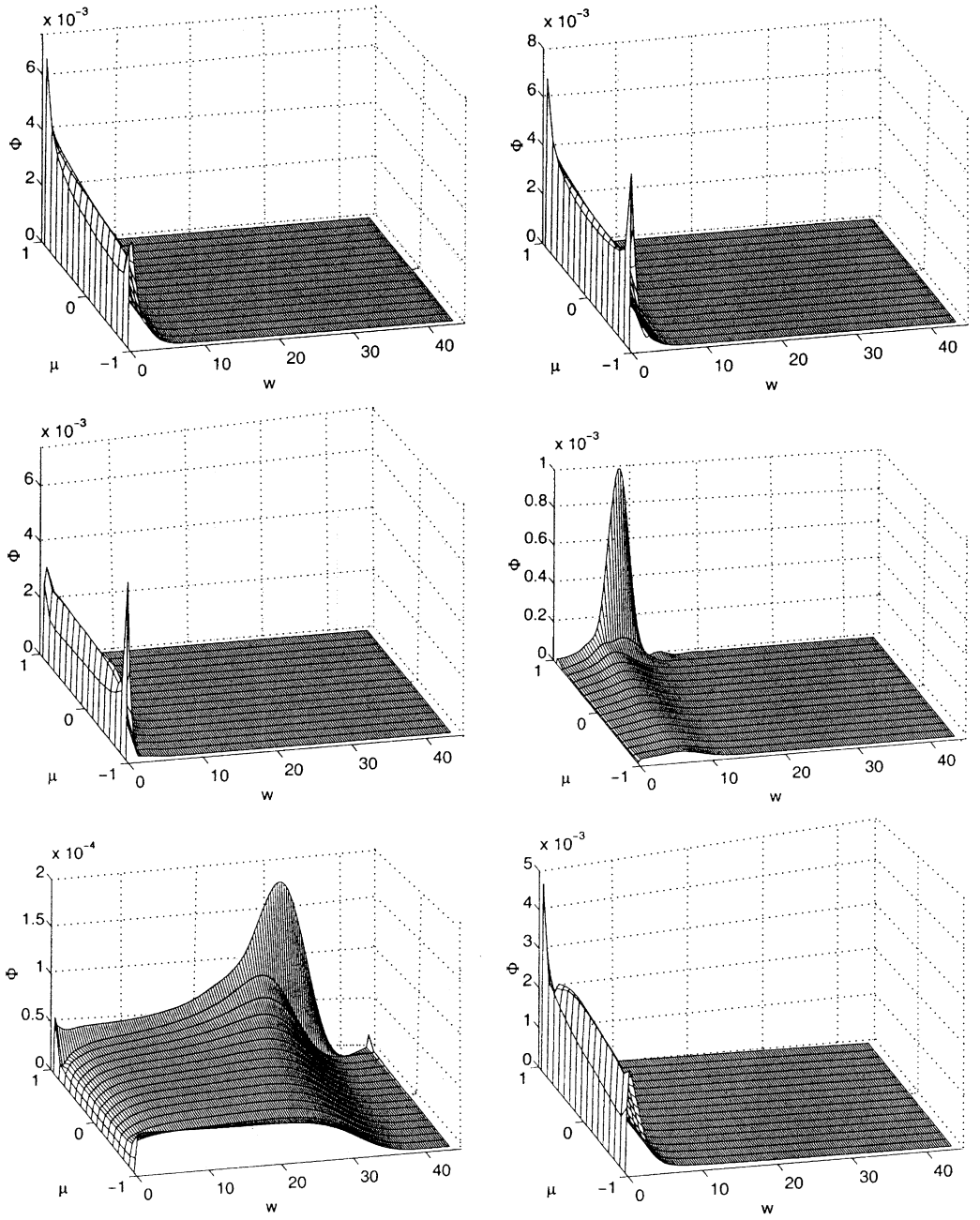

Fig. 2. Spatial snapshots of the steady-state pdf $\Phi_\infty(z_0, w, \mu)$ for the 50 nm channel with 1 V V_{bias}. From left to right and from top to bottom at $z_0 = 0.025$, 0.075, 0.100, 0.125, 0.150, and 0.175 μm.

In Figs. 5 and 6 we perform a comparison between the results of the parabolic band approximation and the nonparabolic (Kane) band approximation at the level of the averaged quantities: density, mean velocity and energy; and at the level of current–voltage characteristics. Current–voltage characteristics are higher

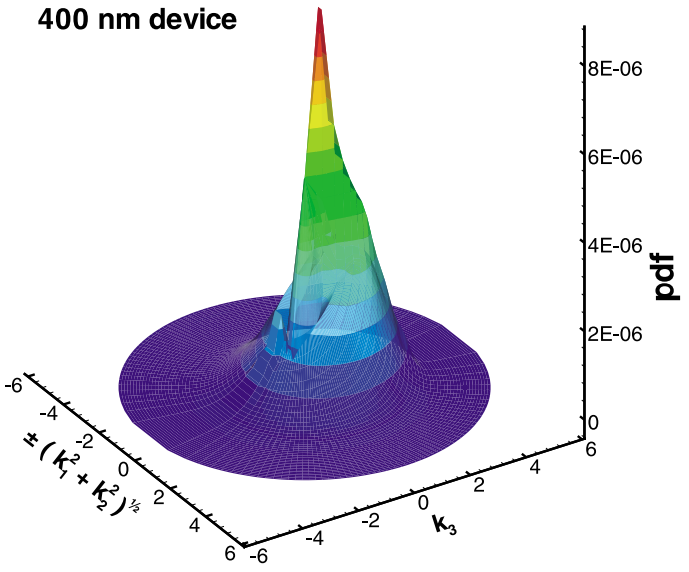

Fig. 3. Pdf $F_\infty(z_0, k)$ for the 400 nm channel with 1 V V_{bias}, in Cartesian coordinates at $z_0 = 0.5\,\mu\text{m}$.

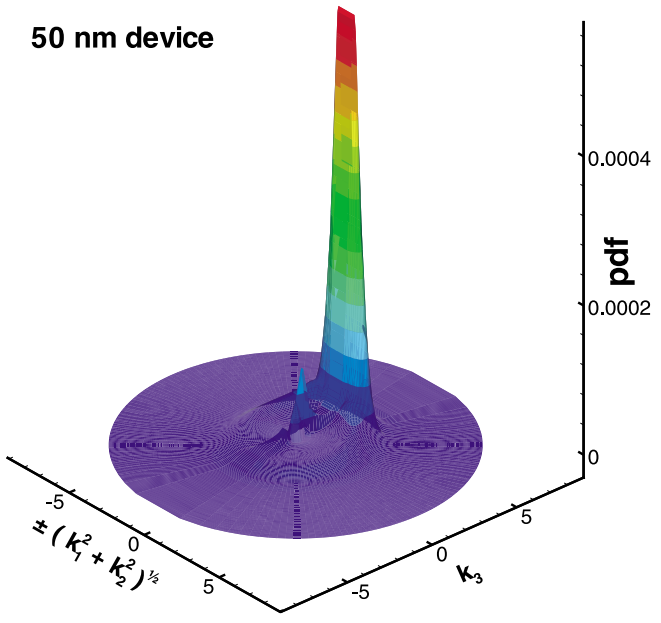

Fig. 4. Pdf $F_\infty(z_0, k)$ for the 50 nm channel with 1 V V_{bias}, in Cartesian coordinates at $z_0 = 0.125\,\mu\text{m}$.

for the parabolic-band case than for the nonparabolic one. Densities are higher for the parabolic-band case near the second junction and mean velocities are lower throughout the channel.

Finally, we show in Figs. 7 and 8 the comparison between the results with the grids specified above and the results of coarser grids. In fact, we take just $100 \times 20 \times 8$ for the 400 nm channel and $60 \times 36 \times 8$ for the 50 nm channel. It is important to assess the resolution of such coarse meshes with a very fast run; let us just mention

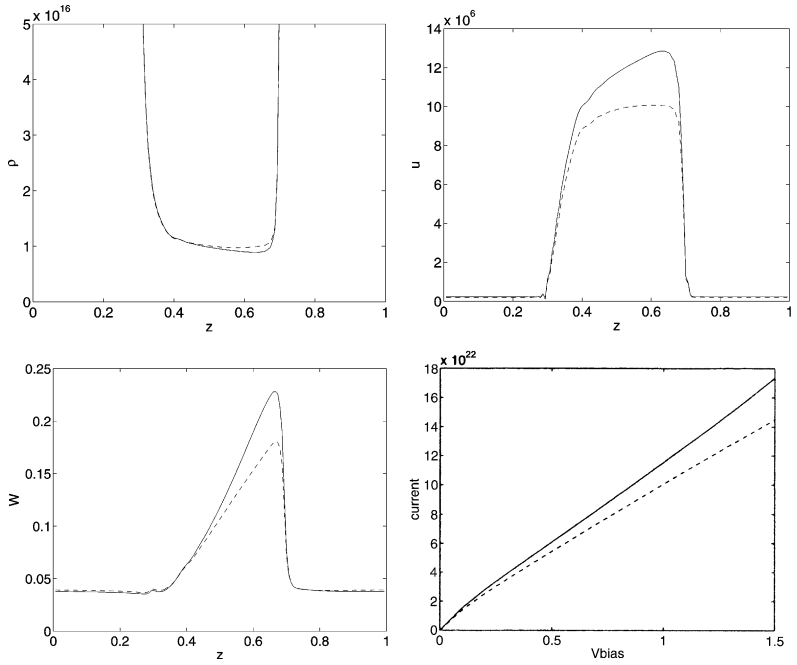

Fig. 5. Comparison of macroscopic density, mean velocity and energy for the 400 nm channel at 1 V V_{bias}, and their IV-curves between the nonparabolic band (dashed line) and the parabolic band (solid line). Top left: density ρ in cm^{-3}; top right: mean velocity u in cm/s; bottom left: energy W in eV; bottom right: current–voltage curves in $\text{cm}^{-2}\,\text{s}^{-1}$ versus V.

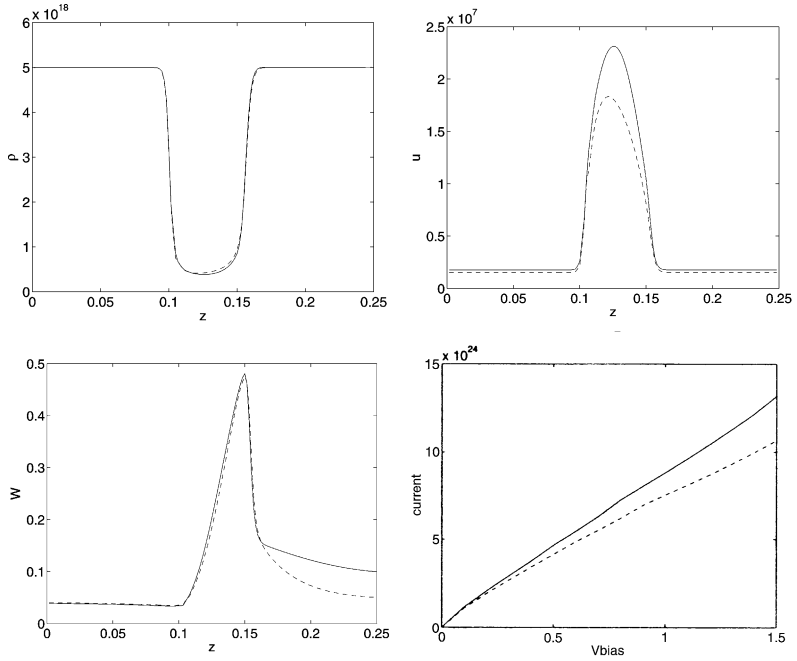

Fig. 6. Comparison of macroscopic density, mean velocity and energy for the 50 nm channel at 1 V V_{bias}, and their IV-curves between the nonparabolic band (dashed line) and the parabolic band (solid line). Top left: density ρ in cm^{-3}; top right: mean velocity u in cm/s; bottom left: energy W in eV; bottom right: current–voltage curves in $\text{cm}^{-2}\,\text{s}^{-1}$ versus V.

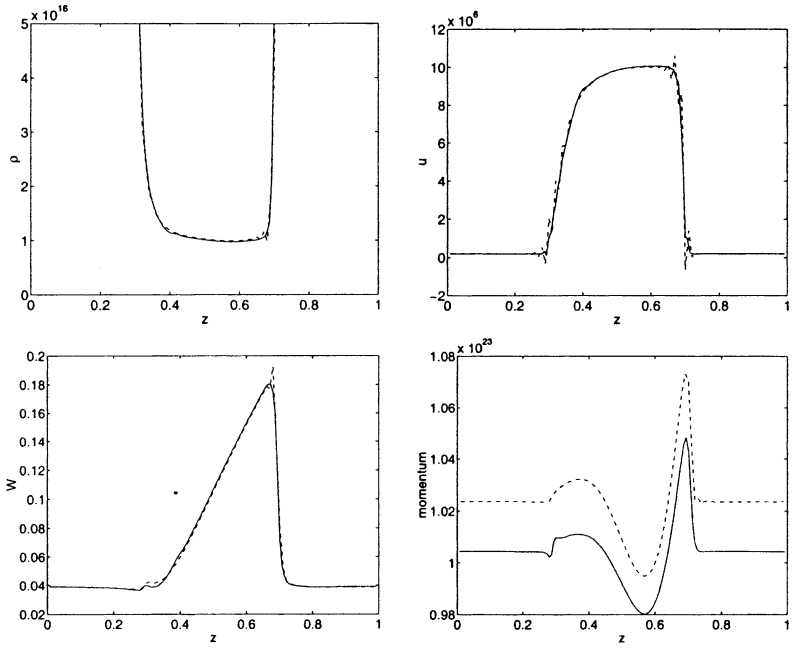

Fig. 7. Comparison of macroscopic quantities for the 400 nm channel at 1 V V_{bias}, between a coarse grid (dashed line) and a finer grid (solid line). Top left: density ρ in cm^{-3}; top right: mean velocity u in cm/s; bottom left: energy W in eV; bottom right: momentum in $\text{cm}^{-2}\,\text{s}^{-1}$.

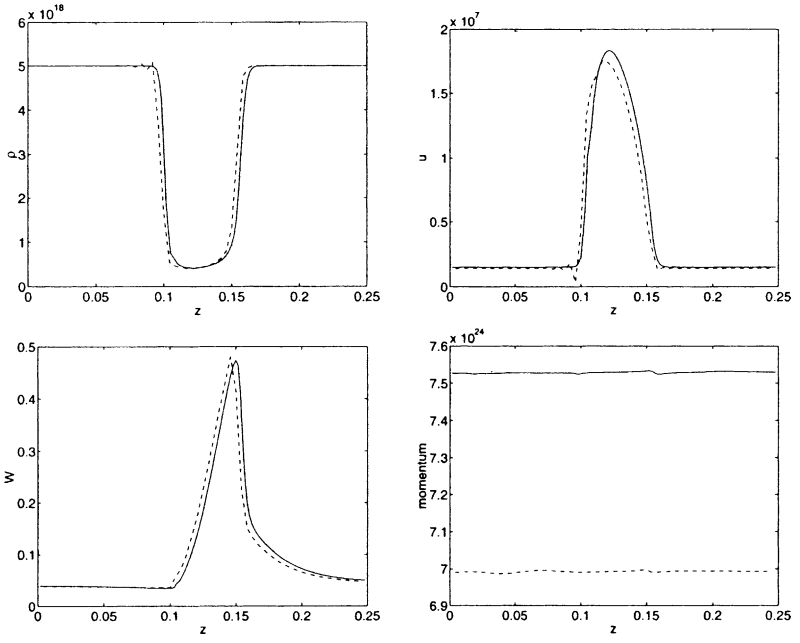

Fig. 8. Comparison of macroscopic quantities for the 50 nm channel at 1 V V_{bias}, between a coarse grid (dashed line) and a finer grid (solid line). Top left: density ρ in cm^{-3}; top right: mean velocity u in cm/s; bottom left: energy W in eV; bottom right: momentum in $\text{cm}^{-2}\,\text{s}^{-1}$.

that the runs for the coarser grids are 10 times faster that the runs for the finer grids. This means about 4 min in a Pentium III 500 MHz versus 40 min for the 400 nm channel and 12 min versus 2 h for the 50 nm channel.

Despite of the oscillations near the junctions we have a very good overall agreement with the finer grid results. This fact is very encouraging and it makes plausible and feasible the generalization of our approach to 2-D devices that is currently under consideration.

4. Transients for diodes

In this section we focus on the time-dependent features of the relaxation towards steady states in the same devices as in the previous section. We only show results for the 400 and 50 nm channel length with the same grids, data and specifications as explained above in the nonparabolic band case with the Kane dispersion relation.

Since our deterministic code allows us to plot pdf at certain locations in the device, we plot the evolution in time of the pdf at the middle of the channel for both cases in Figs. 9 and 10. In both cases, we realize that purely kinetic effects appear in some of the plots, for instance, very asymmetrical distributions appear (remember $\mu = 1$ is the direction of the force field and $\mu = -1$ is the opposite one). In the 400 nm channel, the code has been run till 5 ps, we show results only till 3 ps since later changes are minor. Analogously, for the 50 nm channel we have plotted results only till 1.5 ps although it has been run till 2 ps. We also observe that relaxation time towards steady state is much shorter for the 50 nm channel than for the 400 nm channel, as one could expect.

Evolution of macroscopic quantities: density ρ, mean velocity u, energy W, and momentum is plotted in Figs. 11 and 13 for both channel lengths. We can deduce from these figures the existence of steep gradient regions for all of these average quantities and the transient behaviors in density, mean velocity and energy. Also, plots show that relaxation times for density, mean velocity and energy are in increasing order. Energy takes more time to stabilize (see Figs. 11 and 13, bottom left) than mean velocity. We remind the reader that although the runs have been performed till 5 ps for the 400 nm case and till 2 ps for the 50 nm case, we have plotted the results till the changes in time are irrelevant. In the 400 nm case we can see the existence of a wave in mean velocity and energy traveling clearly from left to right in the early stages of the evolution. In the 50 nm case we see that the mean velocity gets more symmetrical as time evolves.

Also we have plotted the time evolution of the momentum. The momentum is known to be constant at the steady state for a 1-D device. Therefore, we could use this fact to assess the convergence towards steady state during the time evolution. We can see that the numerical flux for the z-direction (the numerical momentum) settles down very well when time increases, especially in an average sense, with the largest residue at the two junctions. Notice that one should always plot the numerical flux, which is the numerical approximation to the momentum, rather than a re-computed momentum based on the numerically obtained density and velocity: see Fig. 12 for the difference. We remark that the WENO scheme, having a smooth numerical flux function, is well suited for steady-state calculations using a time evolution. We also remark that, even with a truly steady-state solver, an iterative procedure is usually still needed to solve the linear or nonlinear system, and convergence is usually also measured in an average sense.

5. Comparisons to other approximate models

This section is devoted to comparisons to other classical approximations that have been used in the literature. First, we review very quickly these models and then, we show their performance against our solver. Simulations to these approximate models are also performed using WENO or ENO schemes. The last part of this section will be devoted to comparisons to DSMC results.

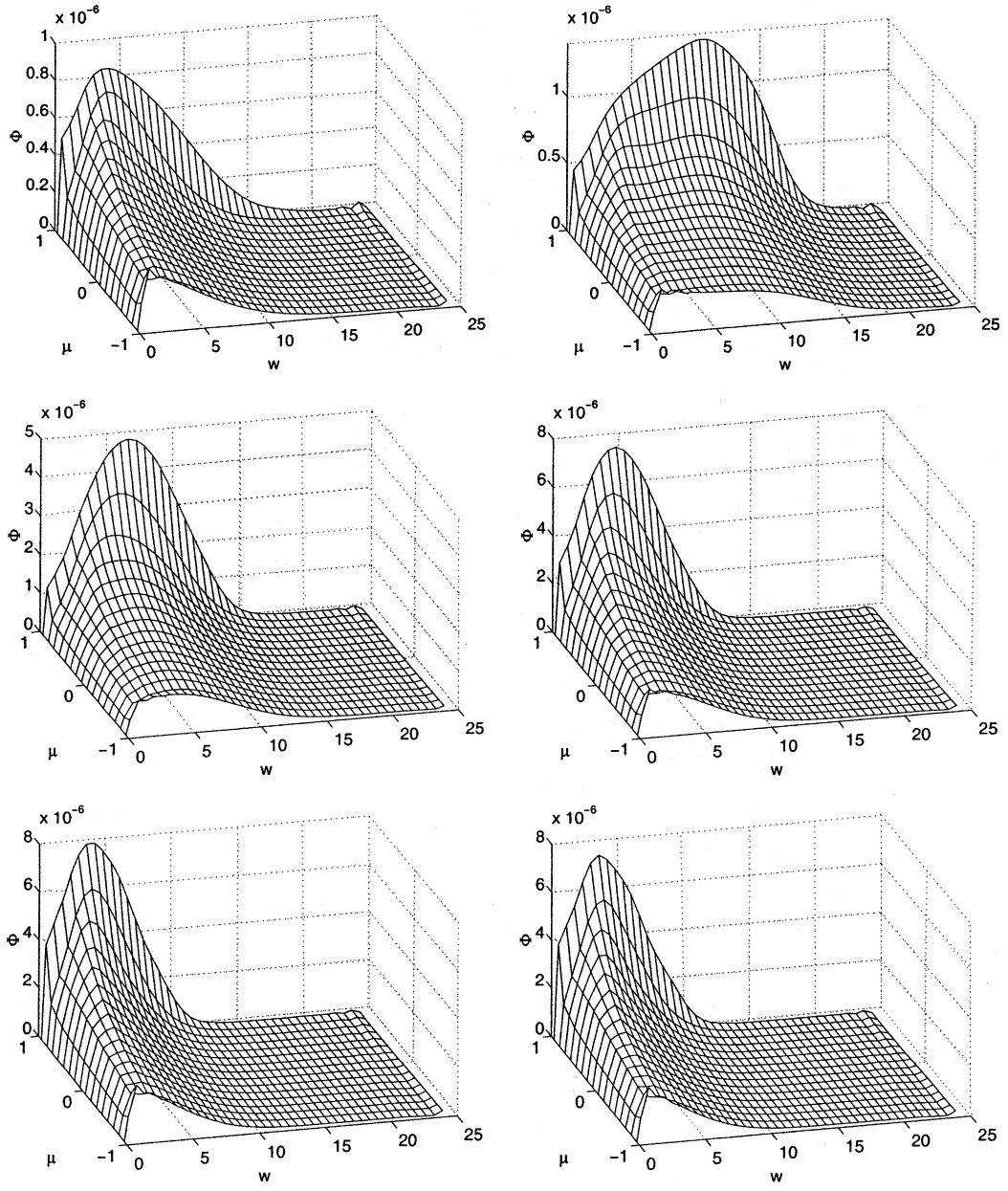

Fig. 9. Time evolution of the pdf $\Phi(t_0, z_0, w, \mu)$ for the 400 nm channel with 1 V V_{bias}, at $z_0 = 0.5\,\mu\text{m}$ from left to right and from top to bottom at times $t_0 = 0.5$, 1.0, 1.5, 2.0, 2.5, and 3.0 ps.

5.1. Relaxation-time kinetic system

Let us consider the following simplified one space dimensional relaxation-time approximation [5,17] to the BTE along flow lines in the direction of the field, that means the wavevector is given by $v = \hbar k_3/m$

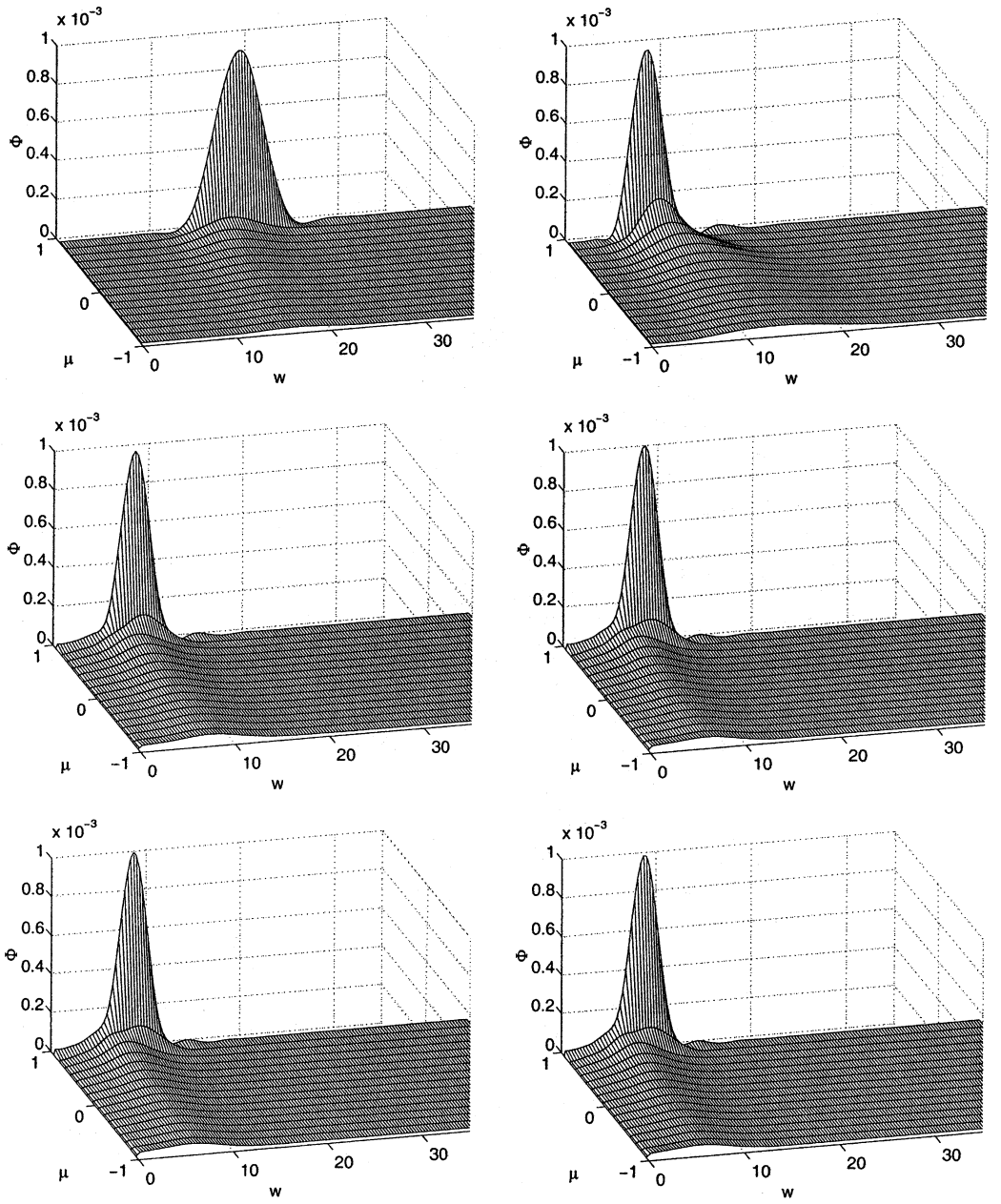

Fig. 10. Time evolution of the pdf $\Phi(t_0, z_0, w, \mu)$ for the 50 nm channel with 1 V V_{bias}, at $z_0 = 0.125\,\mu\text{m}$ from left to right and from top to bottom at times $t_0 = 0.1$, 0.2, 0.4, 0.6, 0.8, and 1.0 ps.

$$\frac{\mathrm{d}f}{\mathrm{d}t} + v f_z - \frac{\mathrm{e}}{m^*} E(t,z) f_v = \frac{1}{\tau}\left(M_{\Theta_{\mathrm{L}}}\rho(f) - f\right) \tag{16}$$

with E given by Poisson equation

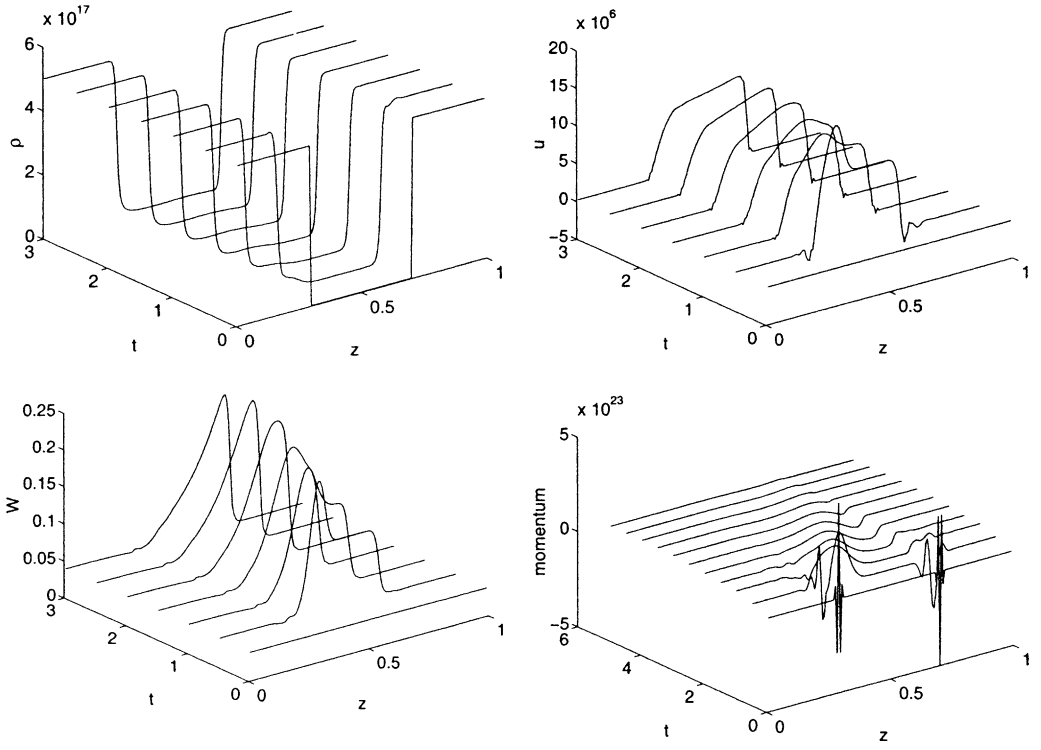

Fig. 11. Evolution of macroscopic quantities for the 400 nm channel at 1 V V_{bias}. Top left: density ρ in cm^{-3}; top right: mean velocity u in cm/s; bottom left: energy W in eV; bottom right: momentum in $\text{cm}^{-2}\,\text{s}^{-1}$.

$$V_{zz} = \frac{\mathrm{e}}{\epsilon}[\rho(t,z) - N_{\mathrm{D}}(z)], \quad E(t,z) = -\Psi_z. \tag{17}$$

Here, the relaxation time $\tau = \tau(|E|)$ depends on the absolute value of the force field in such a way that the drift speed $\frac{\mathrm{e}}{m^*}\tau(|E|)E$ is linear for small values of $|E|$ with slope χ_0 (low-field mobility) and has a horizontal asymptote v_s as $|E|$ becomes large (saturation speed). $M_{\Theta_{\mathrm{L}}}$ is the absolute Maxwellian given by

$$M_{\Theta_{\mathrm{L}}} = (2\pi\Theta_{\mathrm{L}})^{-1/2}\exp\left(-\frac{v^2}{2\Theta_{\mathrm{L}}}\right),$$

where Θ_{L} is the lattice temperature, that is, $\Theta_{\mathrm{L}} = \frac{k_{\mathrm{B}}}{m^*}T_{\mathrm{L}}$. For silicon devices a good approximation [5,4,24] of the mobility based on previous considerations is

$$\frac{\mathrm{e}}{m^*}\tau(t,x) = \frac{2\chi_0}{1+\sqrt{1+4\left(\frac{\chi_0}{v_s}E(t,x)\right)^2}}, \tag{18}$$

where $\chi_0 = 1400\,\text{cm}^2/\text{V s}$ and $v_s = 1.03\ 10^7\,\text{cm/s}$. Systems (16) and (17) will be referred as the RP system. A WENO solver for this system was introduced in [6].

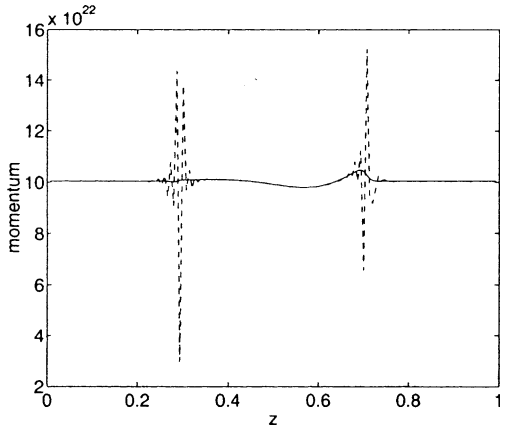

Fig. 12. Comparison of the momentum after 5 ps for the 400 nm channel in the z-direction by the WENO numerical flux (solid line) and by directly computing numerically the corresponding integral of the pdf (dashed line).

5.2. Classical hydrodynamic system

Another simplified classical model is based on taking moments over the BP system and obtaining a close system of equations for the evolution of density, mean velocity and energy after some closure assumption. Hydrodynamic models have been extensively studied in the last few years and corrections to

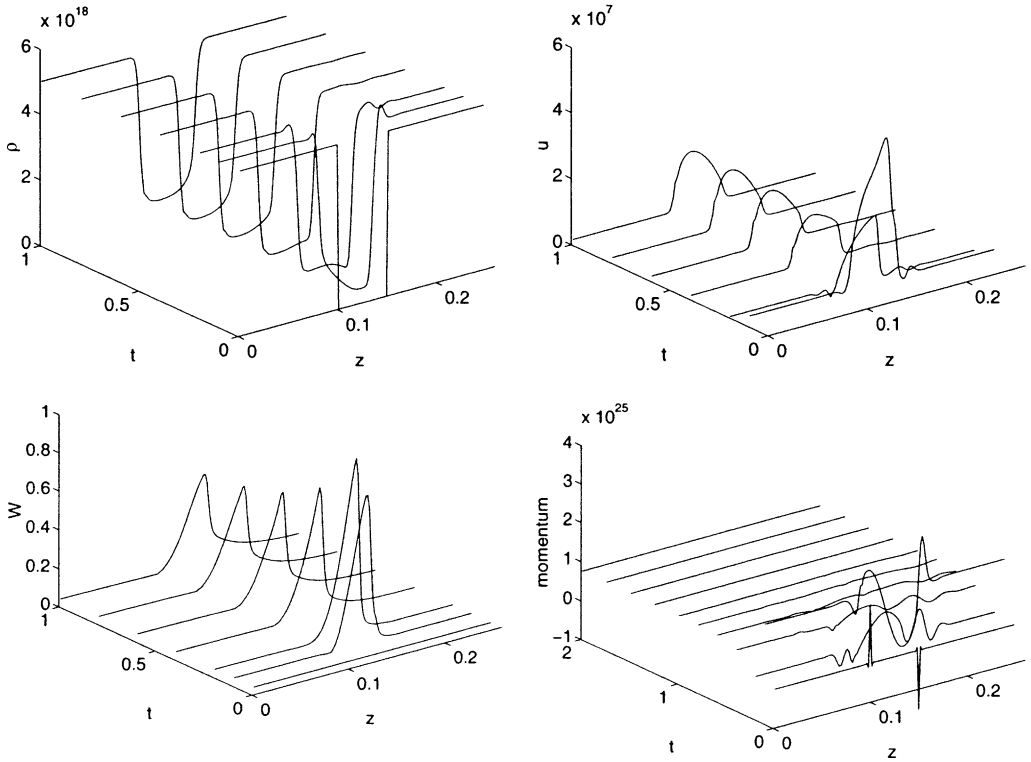

Fig. 13. Evolution of macroscopic quantities for the 50 nm channel at 1 V V_{bias}. Top left: density ρ in cm^{-3}; top right: mean velocity u in cm/s; bottom left: energy W in eV; bottom right: momentum in $\text{cm}^{-2}\,\text{s}^{-1}$.

classical hydrodynamic models have been proposed [1,24] and references therein. Here, we consider only the classical models introduced by Baccarani, Woderman, and Blotekjaer [2,3] that were numerically studied in [12] by ENO methods. These models are derived from a Grad's moment closure method which relies on the fact that the pdf is a shifted Maxwellian and other considerations that assume the Fourier heat flux law combined to the Franz–Wiederman law for the local temperature of the device. This classical system reads

$$\rho_t + (\rho u)_z = 0, \tag{19}$$

$$(\rho u)_t + (\rho u^2 + p)_z = -\frac{\mathrm{e}}{m^*} E\rho - \frac{1}{\tau_m}\rho u, \tag{20}$$

$$(\rho W)_t + (uW + up + q)_z = -\frac{e}{m} E\rho u - \frac{1}{\tau_w}\rho(W - W_{\mathrm{L}}), \tag{21}$$

where W is the energy density per particle

$$W = \frac{3}{2}k_{\mathrm{B}}T + \frac{1}{2}m^*u^2 = \frac{3}{2}\frac{p}{\rho} + \frac{1}{2}m^*u^2,$$

where p is the pressure $p = \rho k_{\mathrm{B}}T$, T is the temperature, and W_{L} is the lattice energy $W_{\mathrm{L}} = \frac{3}{2}k_{\mathrm{B}}T_{\mathrm{L}}$. The heat flux q is assumed to satisfy Fourier's law

$$q = -\kappa\rho T_z.$$

The momentum relaxation time τ_m, energy relaxation time τ_w, and heat flux coefficient κ are given by

$$\tau_{\mathrm{m}} = \frac{m^*\chi_0 T_{\mathrm{L}}}{\mathrm{e}T},$$

$$\tau_w = \chi_0 T_{\mathrm{L}}\left(\frac{m^*}{2\mathrm{e}T} + \frac{3k_{\mathrm{B}}T}{2\mathrm{e}v_s^2(T + T_{\mathrm{L}})}\right),$$

and

$$\kappa = \frac{3}{2}k_{\mathrm{B}}^2\frac{\tau_m T}{m^*}.$$

Here, the values of the low-field mobility χ_0 and saturation speed v_s are the same as in the relaxation-time operator. Of course, Eqs. (19)–(21) are coupled with Poisson equation

$$V_{zz} = \frac{\mathrm{e}}{\epsilon}[\rho(t,z) - N_{\mathrm{D}}(z)], \quad E(t,z) = -\Psi_z. \tag{22}$$

The whole hydrodynamic system (19)–(22) will be referred as the HDP system.

5.3. Drift-diffusion equations

The drift-diffusion-Poisson (DDP) system is an approximation of both the BP system and the relaxation-time system [5,17]. It gives an evolution for the macroscopic density of electrons governed by

$$\rho_t = \partial_z\left(\frac{\mathrm{e}}{m^*}\tau\rho E + \tau\Theta_{\mathrm{L}}\rho_z\right), \tag{23}$$

$$V_{zz} = \frac{\mathfrak{e}}{\epsilon}[\rho(t,z) - N_{\mathrm{D}}(z)], \quad E(t,z) = -\Psi_z. \tag{24}$$

Here, we consider the same mobility model (18) as for the relaxation-time system.

All previous systems have been numerically simulated and compared at the final time achieved for the 400 and 50 nm channel length diodes, i.e., 5 and 2 ps, respectively. The numerical simulation is based again in WENO and ENO methods and we refer to [5,12] for details. The results are shown in Figs. 14 and 15.

From our comparisons, we can infer the validity of macroscopic expansions depending on the length device for the given physical parameters associated to it. In the 400 nm Si channel, Fig. 14 shows that drift diffusion (DDP) and relaxation (RP) models capture well enough the concentration and underestimate the mean velocity, however the (RP) model grossly underestimates the energy, due to the fact that optical-phonon collisions take over and they are not accounted for in the relaxation approximation model (RP).

On the other hand, the hydrodynamic model (HDP) does not do a good job for any of the moments. The spikes showing in the computation of the density and mean velocity ('velocity overshoot') are well known effects due to the nature of the closure which is usually under the assumption that the corresponding pdf is a shifted Maxwellian. In fact the stationary pdf at the center of the channel, Fig. 3 shows the nature of the

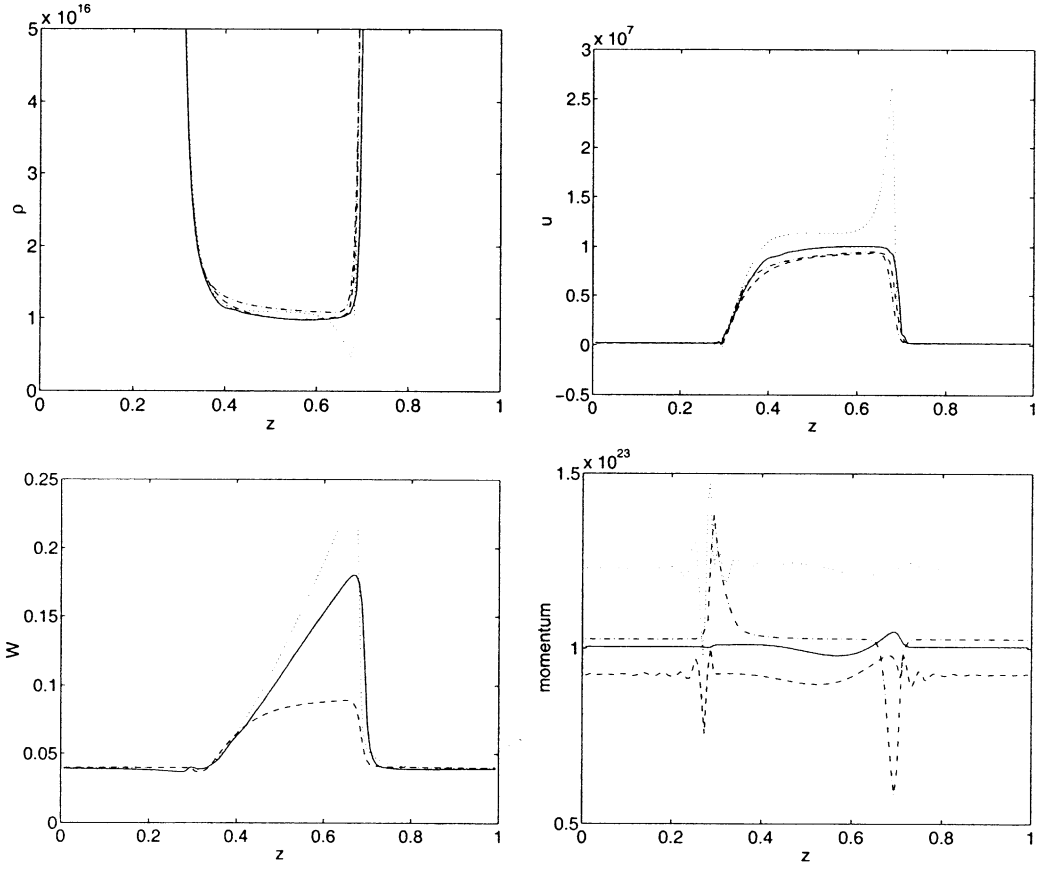

Fig. 14. Comparisons for the 400 nm channel at 1 V V_{bias}, between the full BP system (solid line), relaxation-time kinetic RP system (dashed line), classical hydrodynamic system HDP (dotted line) and drift-diffusion DDP system (dash-dotted line): top left: zoom of density ρ in cm^{-3}; top right: mean velocity u in cm/s; bottom left: energy W in eV; bottom right: momentum in $\mathrm{cm}^{-2}\,\mathrm{s}^{-1}$.

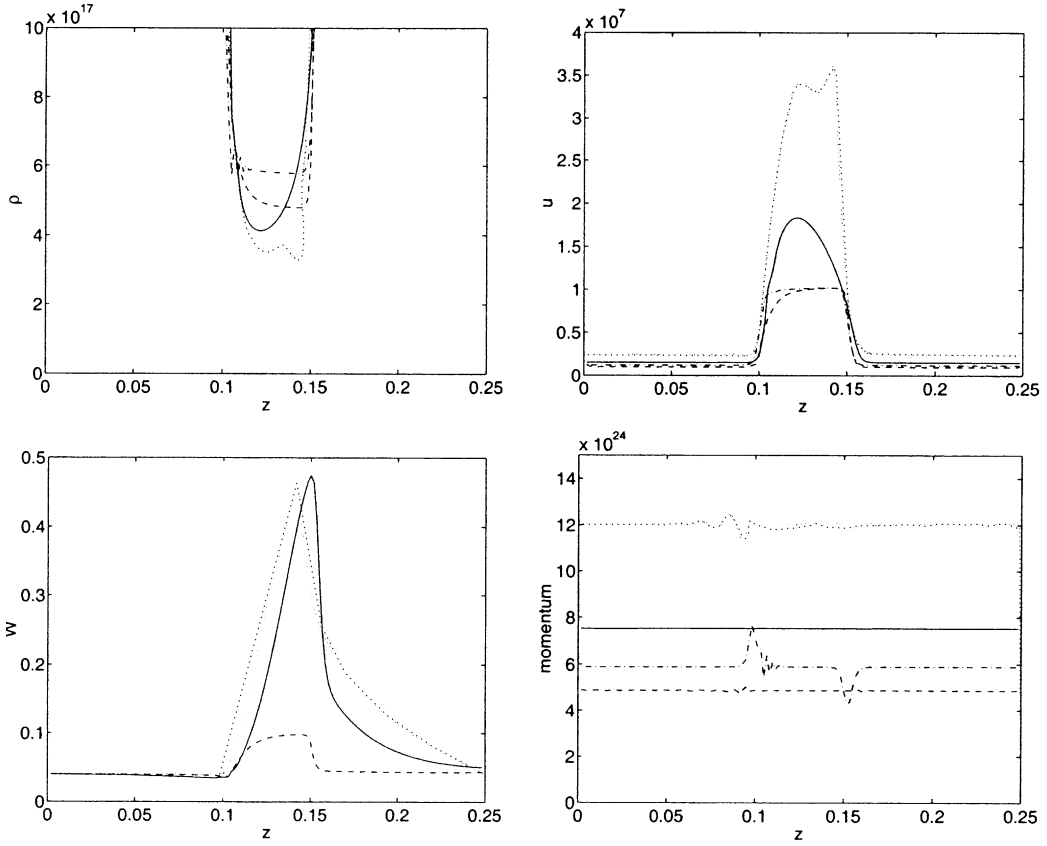

Fig. 15. Comparisons for the 50 nm channel at 1 V V_{bias}, between the full BP system (solid line), relaxation-time kinetic RP system (dashed line), classical hydrodynamic system HDP (dotted line) and drift-diffusion system DDP (dash-dotted line): top left: zoom of density ρ in cm^{-3}; top right: mean velocity u in cm/s; bottom left: energy W in eV; bottom right: momentum in $cm^{-2}\,s^{-1}$.

anisotropy, which makes a gross deviation from a Maxwellian state. Even though these spikes can be "eliminated" by several methods which involve fitting of parameters, we have not taken them into account here.

We point out that a consequence of our deterministic computation is the need of a major correction to the derivation of hydrodynamic closures for charged transport in inhomogeneous structures, even at the 0.4 μm scale, where they are currently accepted.

Clearly, for the 50 nm channel, it becomes imperative to abandon any classical macroscopic approximation based on either hydrodynamics or relaxation as seen in Fig. 15. Energy becomes too large and the stationary pdf, as shown in Fig. 4, becomes multi mode and too anisotropic to be captured by an evolution of spatial variations of statistical approximations to its moments.

This is a clear evidence of the need of domain decomposition coupling kinetic and macroscopic deterministic computations to incorporate higher dimensional space inhomogeneities.

5.4. DSMC simulations

We compare Monte Carlo simulations (DSMC) with BP results, in Figs. 16–19. The scattering and the physical parameter used in both cases are the same. This is essential to meaningful comparisons. The only

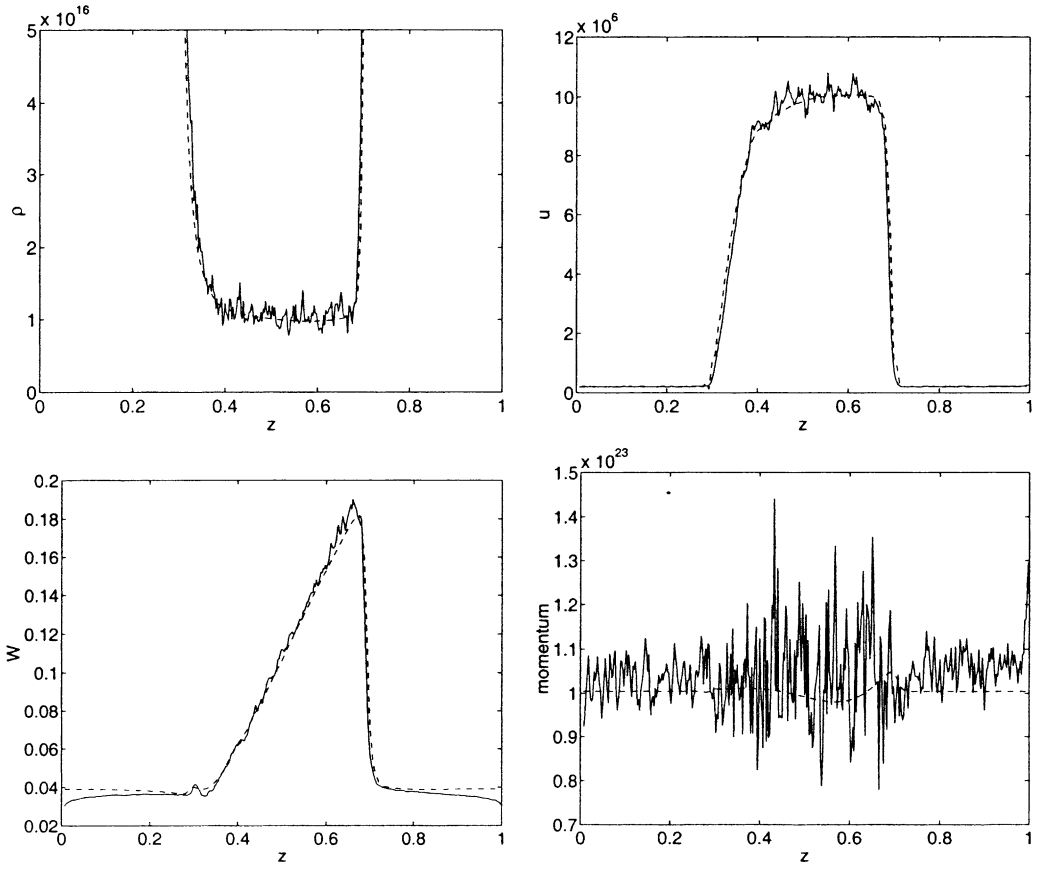

Fig. 16. Comparisons for the 400 nm channel at 1 V V_{bias}, between the full BP system by the DSMC method (solid line) and by the deterministic WENO solver (dashed line): top left: zoom of density ρ in cm^{-3}; top right: mean velocity u in cm/s; bottom left: energy W in eV; bottom right: momentum in $cm^{-2}\,s^{-1}$.

difference is in the spatial boundary conditions. For the DSMC the particle behavior at the boundaries is driven by the assumption of a local charge neutrality and thermal equilibrium. In particular, after each time step, charge neutrality is examined at boundaries. If in a boundary cell we have a net accumulation of charge greater then the target density, some particles will leave the device. Otherwise, some particles should be injected into the device only if this addition will reduce the net deviation from the charge neutrality. Having decided to add a particle, its velocity must be directed into the devices and its energy chosen randomly but according a Maxwellian distribution. We remark that in the n_+–n–n_+ diode boundary cells lie in high doping regions, so only a few particles enter or leave for every time step, since the n_+ regions are regions of quasi neutral charges away from the junctions. Thus, the entering particles modify the carrier distribution only near the boundaries. Boundary conditions for BP should take into account the characteristic information of the streaming operator. However, to stay as close to the numerical boundary conditions adopted in the DSMC as possible for the purpose of a comparison, we have used a reflecting boundary condition for the inflow and Neumann type boundary condition for the outflow.

The boundary conditions for DSMC are simple and reasonable, but they are not completely justified by means of physical or mathematical arguments. We note, in fact, that drifted Maxwellian distributions are

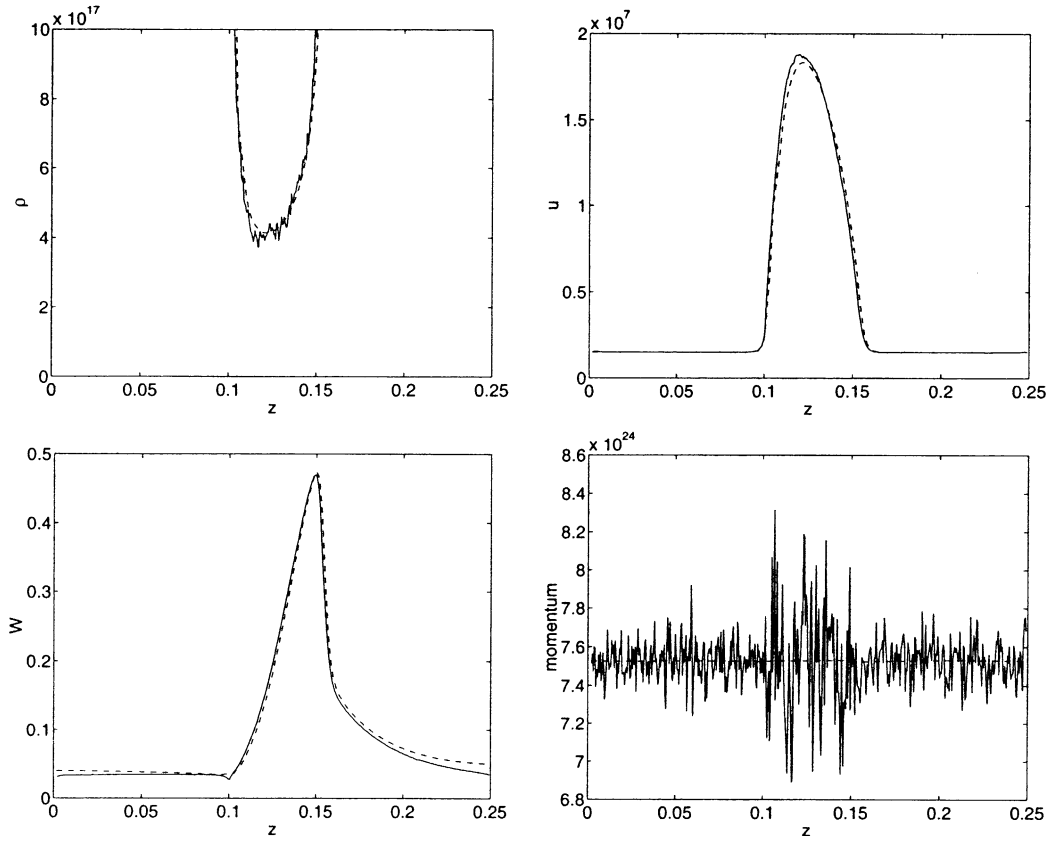

Fig. 17. Comparisons for the 50 nm channel at 1 V V_{bias}, between the full BP system by the DSMC method (solid line) and by the deterministic WENO solver (dashed line): top left: zoom of density ρ in cm^{-3}; top right: mean velocity u in cm/s; bottom left: energy W in eV; bottom right: momentum in $cm^{-2}\,s^{-1}$.

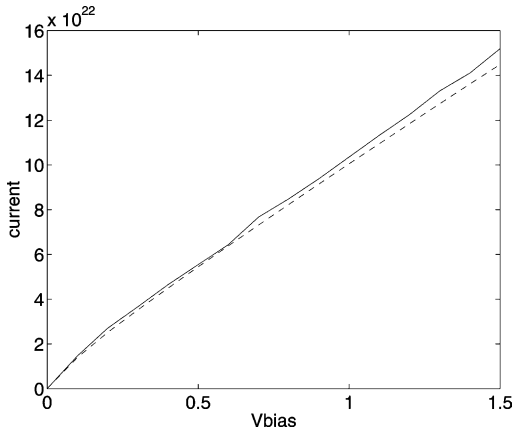

Fig. 18. Comparison of the IV-curves between the deterministic WENO solver (dashed line) and the DSMC method (solid line) for the 400 nm channel.

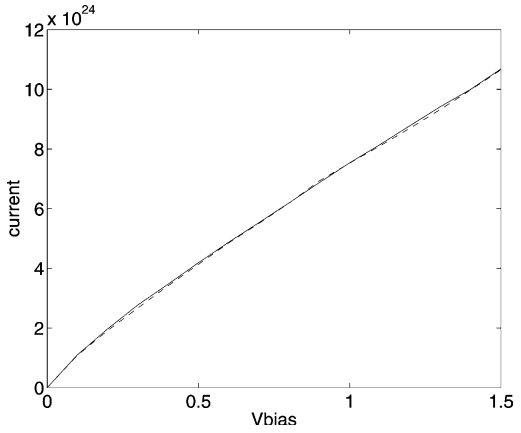

Fig. 19. Comparison of the IV-curves between the deterministic WENO solver (dashed line) and the DSMC method (solid line) for the 50 nm channel.

real static and stationary solutions of the Boltzmann equations in the case of perfect gas, where only particle-particle scattering is considered. These solutions, which give a vanishing collision integral, are also related to the entropy through H-Theorem and to asymptotic behavior of time-dependent solutions. In this paper the Boltzmann equation (1) describes the evolution of an electron gas inside a crystal and only electron–phonon scattering is taken into account. Now, following [14] the equation $Q(f) = 0$ gives again a Maxwellian distribution function, but having null drift velocity and the same temperature of the lattice. Moreover, there exist other infinite solutions given by the product of the above Maxwellian and an arbitrary periodic function of ε with period equal to $\hbar\omega$. Hence, drifted Maxwellian is not a mathematical or physical solution of Eq. (1). The only physical argument to justify the choice of these boundary conditions for DSMC simulations is the following: The electrons are injected into the semiconductor through a contact, where we assume that the electrons move freely or collide only with other electrons. So, it is clear that we are neglecting interactions with the other particles of the contact and assuming that the injected electrons have the same temperature of the lattice. Of course this is only an approximation. In principle the problem of a correct distribution of injected electrons can be solved by introducing a transport equation for these and suitable boundary conditions in the contact.

In Monte Carlo (DSMC) simulations particles have one spatial component z and three dimensions for the wavevector k. It is thus a time plus one spatial dimension plus three wave dimension simulation. Let τ be the mean free time. Each particle has its own mean free time, which changes randomly after every collision. The particle moves (drift motion) in 1-D space according to the Newton's law, where the force is exactly the z-component of the electric field evaluated by solving the Poisson equation, during an interval having τ length. During this time of free flight only the spatial coordinate and z-component of the velocity change (this involves both the third component of k and the electron energy, since we are considering the Kane model). After this time step, for fixed time and space, particles collide according to the probability of scattering. Hence, only the energy of the particle changes and therefore the three components of the wavevector. This makes reasonable the comparison with the WENO-solver of BP.

The comparisons between BP and DSMC show a very good agreement, particularly for the IV-curves in Figs. 18 and 19, which are averaged quantities. The most noticeable difference is in the energy plots (Figs. 16 and 17, lower left graphs) near the boundaries. This is probably due to the fact that in DSMC electrons are injected according to a Maxwellian distribution. We note that, for the smaller device, the electric fields are very strong. In fact, the velocity in the center of the diode is almost twice the saturation velocity. Nevertheless, we obtain smooth solutions from the BP simulations. On the other hand, the DSMC results

are very noisy. Also for such 1-D devices, the deterministic BP simulations by our WENO solver is much faster than the DSMC simulations. As we mentioned before, the deterministic BP simulations also have the advantage of easy comparisons with hydrodynamic and other moment models, accurate solutions both for large or small electric field (the small electric field case is difficult for DSMC due to the noises), easiness for time transient simulations, and for the determination of scattering parameters (these parameters often need to be changed in order to fit the experimental data).

As a final remark, we point out that our results show the possibility that, also in the case of electron kinetic theory, a convergence theorem of Monte Carlo dynamics to the Boltzmann equation may be established.

6. Conclusions

We have developed a new deterministic simulation tool for the one spatial dimensional Boltzmann Poisson system, based on a high order WENO scheme, and performed a detailed study of numerical comparisons between our deterministic simulation tool and the DSMC simulations as well as various other simplified models. This new deterministic simulation tool allows the evaluation of the electron probability density function (pdf) for plasma simulations at nano scales and provides a calibrator of stationary non-statistical-equilibrium states and their corresponding macroscopic approximations for the evolution of their observable quantities. It becomes a reliable bench mark for determining the range of validity of moments equations for a given channel and voltage bias. It is also a more informative tool, capable of computing transients for the pdf, at a much smaller cost than the classical Monte Carlo solvers to obtain reliable and not noisy data for the 1-D devices. Higher dimensional extensions of the WENO solver for the Boltzmann Poisson system are currently under way.

Acknowledgements

The first author is supported by the DGI-MCYT/FEDER Project BFM2002-01710 and the European IHP Network HYKE Project HPRN-CT-2002-00282. The second author is supported by NSF under Grant DMS 9971779 and by TARP under Grant 003658-0459-1999. The third author is supported by Italian MIUR and by the IHP Project "HYKE" HPRN-CT-2002-00282. Research of the fourth author is supported by NSF Grant ECS-9906606 and ARO Grant DAAD19-00-1-0405. We thank TICAM at The University of Texas at Austin for partially supporting this research.

References

[1] A.M. Anile, V. Romano, G. Russo, Extended hydrodynamical model of carrier transport in semiconductors, SIAM J. Appl. Math. 61 (2000) 74–101.
[2] G. Baccarani, M.R. Woderman, An investigation of steady state velocity overshoot effects in Si and GaAs devices, Solid State Electron. 28 (1985) 407–416.
[3] K. Blotekjaer, Transport equations for electrons in two-valley semiconductors, IEEE Trans. Electron Dev. 17 (1970) 38–47.
[4] J.A. Carrillo, I.M. Gamba, O. Muscato, C.-W. Shu, Comparison of Monte Carlo and deterministic simulations of a silicon diode, IMA Volumes in Mathematics and Its Applications (to appear).
[5] J.A. Carrillo, I.M. Gamba, C.-W. Shu, Computational macroscopic approximations to the 1-D relaxation-time kinetic system for semiconductors, Physica D 146 (2000) 289–306.
[6] C. Cercignani, I.M. Gamba, J.W. Jerome, C.-W. Shu, Device benchmark comparisons via kinetic, hydrodynamic, and high-field models, Comput. Meth. Appl. Mech. Eng. 181 (2000) 381–392.
[7] P. Degond, F. Delaurens, F.J. Mustieles, Semiconductor modelling via the Boltzmann equation, Comput. Meth. Appl. Sci. Eng. (1990) 311–324.

[8] F. Delaurens, F.J. Mustieles, A deterministic particle method for solving kinetic transport equations: the semiconductor Boltzmann equation case, SIAM J. Appl. Math. 52 (1992) 973–998.
[9] E. Fatemi, F. Odeh, Upwind finite difference solution of Boltzmann equation applied to electron transport in semiconductor devices, J. Comput. Phys. 108 (1993) 209–217.
[10] S. Gottlieb, C.-W. Shu, Total variation diminishing Runge–Kutta schemes, Math. Comp. 67 (1998) 73–85.
[11] C. Jacoboni, P. Lugli, The Monte Carlo Method for Semiconductor Device Simulation, Springer, New York, 1989.
[12] J.W. Jerome, C.-W. Shu, Energy models for one-carrier transport in semiconductor devices, in: W. Coughran, J. Cole, P. Lloyd, J. White (Eds.), IMA Volumes in Mathematics and Its Applications, vol. 59, Springer, Berlin, 1994, pp. 185–207.
[13] G. Jiang, C.-W. Shu, Efficient implementation of weighted ENO schemes, J. Comput. Phys. 126 (1996) 202–228.
[14] A. Majorana, Space homogeneous solutions of the Boltzmann equation describing electron–phonon interactions in semiconductors, Transp. Theory Stat. Phys. 20 (1991) 261–279.
[15] A. Majorana, A comparison between bulk solutions to the Boltzmann equation and the spherical harmonic model for silicon devices, in: A.M. Anile, V. Capasso, A. Greco (Eds.), Progress in Industrial Mathematics at ECMI 2000, Mathematics in Industry, vol. 1, Springer, Berlin, 2002, pp. 169–173.
[16] A. Majorana, R. Pidatella, A finite difference scheme solving the Boltzmann–Poisson system for semiconductor devices, J. Comput. Phys. 174 (2001) 649–668.
[17] P.A. Markowich, C. Ringhofer, C. Schmeiser, Semiconductor Equations, Springer, New York, 1990.
[18] K. Rahmat, J. Whithe, D.A. Antoniadis, Simulation of semiconductor devices using a Galerkin/spherical harmonic expansion approach to solving the coupled Poisson–Boltzmann system, IEEE Trans. Comput.-Aid. Des. 15 (1996) 1181–1196.
[19] L. Reggiani, in: Hot-electron transport in semiconductors, Topics in Applied Physics, vol. 58, Springer, Berlin, 1985.
[20] C. Ringhofer, Computational methods for semiclassical and quantum transport in semiconductor devices, Acta Num. 3 (1997) 485–521.
[21] C. Ringhofer, Space–time discretization methods for series expansion solutions of the Boltzmann equation for semiconductors, SIAM J. Num. Anal. 38 (2000) 442–465.
[22] C. Ringhofer, C. Schmeiser, A. Zwirchmayer, Moment methods for the semiconductor Boltzmann equation in bounded position domains, SIAM J. Num. Anal. 39 (2001) 1078–1095.
[23] C. Ringhofer, A mixed spectral-difference method for the steady-state Boltzmann–Poisson system, preprint.
[24] V. Romano, G. Russo, Numerical solution for hydrodynamical models of semiconductors, Math. Mod. Meth. Appl. Sci. 10 (2000) 1098–1120.
[25] C.-W. Shu, Essentially non-oscillatory and weighted essentially non-oscillatory schemes for hyperbolic conservation laws, in: B. Cockburn, C. Johnson, C.-W. Shu, E. Tadmor (Editor: A. Quarteroni) Advanced Numerical Approximation of Nonlinear Hyperbolic Equations, Lecture Notes in Mathematics, vol. 1697, Springer, 1998, pp. 325–432.
[26] C.-W. Shu, S. Osher, Efficient implementation of essentially non-oscillatory shock capturing schemes, J. Comput. Phys. 77 (1988) 439–471.
[27] K. Tomizawa, Numerical simulation of submicron semiconductor devices, Artech. House, Boston, 1993.